remote sensing

MDPI

Article

Ultra-Long-Term InSAR Deformation Assessment Through Statistical Harmonization of Multi-Release EGMS Data and Hydro-Deformation Regime Concordance Analysis

Rasoul Eskandari * and Marco Scaioni

Department of Architecture, Built Environment and Construction Engineering, Politecnico di Milano, via Ponzio 31, 20133 Milano, Italy; marco.scaioni@polimi.it
* Correspondence: rasoul.eskandari@polimi.it

Highlights

What are the main findings?

- Enhanced Temporal Alignment via Statistical Testing (TAST) harmonizes four European Ground Motion Service (EGMS) Ortho releases of the Interferometric Synthetic Aperture Radar (InSAR) products spanning 2016–2024 while preserving their within-release deformation evolution; inter-release velocity discrepancies reached 7.12 mm/y in vertical and 11.21 mm/y in horizontal East–West directions, demonstrating the need for temporal alignment before constructing ultra-long-term (ULT) deformation records.
- The proposed Hydro-Deformation Regime Concordance (HDRC) analysis reveals spatially organized and geologically conditioned hydro-deformation regimes: vertical responses are predominantly anti-concordant with regional groundwater-level turning behavior (59.7–69.9% negative HDRC), whereas E-W responses vary markedly among successive transitions; spatial autocorrelation reaches Moran's $I = 0.51$, geological association Cramér's $V = 0.31$, and geological-group persistence Kendall's W up to 0.88.

What are the implications of the main findings?

- The harmonization framework can be extended directly to subsequent EGMS releases, providing the EGMS-user community with a reusable strategy for progressively constructing temporally consistent, continuously extending deformation records.
- The resulting ultra-long-term records enable phase-dependent investigation of non-stationary deformation processes, allowing recurrent hydro-deformation responses and their geological conditioning to be identified beyond what individual EGMS releases or full-period deformation summaries may reveal.

Check for updates

Academic Editor: Dongping Ming

Received: 8 September 2026
Revised: 7 October 2026
Accepted: 13 October 2026
Published: 18 October 2026

Copyright: © 2026 by the authors. Licensee MDPI, Basel, Switzerland. This article is an open access article distributed under the terms and conditions of the Creative Commons Attribution (CC BY) license.

Abstract

Interferometric Synthetic Aperture Radar (InSAR) products from the European Ground Motion Service (EGMS) are released through successive, partially overlapping temporal windows, offering the potential to construct ultra-long-term (ULT) deformation records, i.e., continuous records spanning multiple releases and exceeding the 5–6-year extent of any individual release. However, direct combination of independently processed releases may introduce artificial offsets and trend changes. This study presents an enhanced Temporal Alignment via Statistical Testing (TAST) procedure to harmonize four EGMS Ortho releases (R1–R4; January 2016–December 2024) over the Lecco–Como area of northern Italy in both Up–Down and East–West components. The method applies translation and linear velocity correction optimized through a joint Cramér–von Mises/RMSE (Root Mean Square Error)

objective while preserving within-release deformation evolution. The resulting ULT records were segmented at three regional groundwater-level (GWL) turning points (TPs) and analyzed using the introduced Hydro-Deformation Regime Concordance (HDRC) metric. The results show that inter-release velocity discrepancies reached 7.12 mm/y in U-D and 11.21 mm/y in E-W, demonstrating their potential to substantially alter apparent long-term deformation regimes. Vertical deformation was predominantly anti-concordant with GWL turning behavior, with 59.7–69.9% negative HDRC, whereas E-W responses evolved from strong positive HDRC dominance to near-balanced conditions. HDRC exhibited significant spatial organization (Moran's I up to 0.51) and geological association (Cramér's V up to 0.31), while geological-group response rankings remained persistent across successive hydro-regime transitions (Kendall's W up to 0.88). A screening of potential alternative regional drivers identified no clear evidence that seismicity, capable faults, or isolated extreme precipitation events accounted for the observed multi-TP patterns. These results demonstrate that systematic multi-release EGMS harmonization enables temporally consistent long-term monitoring and reveals non-stationary, spatially structured, and geologically conditioned deformation responses associated with groundwater dynamics.

Keywords: European Ground Motion Service (EGMS); geological conditioning; groundwater level; InSAR; statistical testing; temporal alignment

1. Introduction

Interferometric Synthetic Aperture Radar (InSAR) has become a key technique for measuring ground deformation over large areas with high spatial density and millimetric sensitivity [1,2]. The systematic Sentinel-1 acquisition strategy has further supported the transition from local investigations towards continuous regional and continental monitoring [3]. The European Ground Motion Service (EGMS) provides standardized, freely accessible deformation time series (DefTS) across Europe and updates them through successive, partial temporal overlapping releases [4,5]. This strategy creates the opportunity to use EGMS as a progressively expanding archive for long-term ground displacement analysis (for further details, see Section 2.2).

Owing to their standardized processing, continental-scale coverage, and consistent quality control, EGMS products have become widely adopted within the deformation monitoring community [6]. They have been successfully exploited for investigating a broad range of geohazards and deformation processes, including land subsidence [7,8], landslides [9,10], earthquake-related deformation [11], and deformation responses associated with extreme meteorological and climatic phenomena [12–14]. Also, they have supported the monitoring of structures [15,16], as well as critical infrastructures [17,18]. Nevertheless, most applications remain release-specific, while the potential of the complete release sequence for continuous deformation analysis remains insufficiently explored.

Some recent studies have begun to compare or jointly exploit multiple EGMS releases. Michalakis and Loupasakis [19] compared two overlapping EGMS releases to assess the consistency of earthquake-related vertical displacement estimates, treating the releases as independent processing generations. Hrysiewicz et al. [20] demonstrated the joint handling of two EGMS releases within the EGMS-toolkit framework, mainly from a data-access and large-scale processing perspective rather than for constructing a temporally continuous deformation record. Eskandari and Scaioni [21] proposed an initial concept for temporal alignment via statistical testing, specifically for EGMS Ortho DefTS. The concept exploits the statistical similarity between DefTS in an overlapping period to align the DefTS of two successive releases (refer to Section 3.2). It is of great importance to

note that the opportunity of continuous monitoring provided by EGMS is not automatic. Successive EGMS releases originate from independent multi-temporal InSAR (MT-InSAR) processing campaigns with different periods, and may differ in deformation level, temporal trend, short-period variability, or statistical distribution (see Section 4.2). It is evident that simple concatenation may introduce artificial offsets or trend changes and may even alter the apparent deformation regime. This bias becomes crucial when the objective is not merely to map the average velocities, but to interpret temporal changes associated with external forcing.

Groundwater-level (GWL) variation provides a relevant setting in which to examine this problem. Variations in hydraulic head modify pore pressure and effective stress and may generate compaction, expansion, subsidence, or uplift [22]. Numerous studies have combined InSAR deformation and groundwater observations to investigate aquifer-system deformation [23], estimate hydro-mechanical properties [24], and assess subsidence or rebound associated with groundwater withdrawal and recovery [25,26]. Importantly, previous studies have demonstrated that groundwater-driven deformation can vary across hydrological phases, with distinct deformation responses emerging during periods of groundwater depletion, stabilization, recovery, and recharge [27–29]. Thus, resolving such phase-dependent behavior requires long-term, temporally consistent DefTS capable of capturing successive hydro-deformation regimes. Furthermore, the deformation response to GWL variations is not spatially uniform and is strongly conditioned by the geological and hydrogeological properties of the aquifer system. Previous studies have shown that lithology, the thickness and distribution of compressible deposits, and structural discontinuities can control the magnitude, timing, reversibility, and spatial extent of groundwater-induced deformation [30,31].

Despite the continuous monitoring opportunities offered by EGMS, the existing literature lacks a contemporary, comprehensive exploitation of systematic harmonization of the complete sequence of available EGMS releases to generate longer-term DefTS, and its application in the investigation of non-stationary hydro-deformation responses and their geological conditioning. The gap is broader than extending temporal coverage: it concerns preserving the internal evolution of each release, correcting inter-release inconsistencies, and converting the resulting long records into interpretable information on environmental deformation processes.

This study addresses this extensive gap, exploiting EGMS Ortho Data in both Up–Down (U-D) and East–West (E-W) datasets over the Lecco–Como sector of northern Italy. An enhanced formulation of Temporal Alignment Via Statistical Testing (TAST) is developed to harmonize four EGMS Ortho releases while preserving their within-release deformation variations. Adjacent raw releases are aligned through translation and linear velocity correction using both distributional and temporal agreement criteria, after which the pairwise transformations are cumulatively propagated into the most recent release frame. The resulting ultra-long-term (ULT) DefTS, covering January 2016–December 2024, is segmented at the principal regional GWL turning points (TPs). The regime changes are quantified through an introduced metric, namely Hydro-Deformation Regime Concordance (HDRC), and are evaluated in terms of spatial integrity, geological conditioning, temporal persistence, and possible alternative regional drivers. The present investigation is structured around the following core research questions:

- Do successive EGMS Ortho releases provide adequate measurement point (MP) continuity, and are their raw inter-release inconsistencies sufficiently large to bias ULT deformation interpretation?

- Can enhanced TAST adjust successive releases while preserving their internal deformation evolution and produce time series with quantifiable consistency within a common reference frame?
- Do the harmonized records reveal spatially organized changes in Up–Down and East–West deformation regimes associated with successive groundwater-level turning points?
- Are the sign and magnitude of these responses conditioned by geological setting, and do geological-group response patterns persist across alternating hydro-regime transitions?

The key contributions of this study are threefold: (i) Methodologically, the proposed framework preserves the within-release nonlinear variations and constructs ULT DefTS in a common reference frame. Here, the term ULT is used in an operational release-relative sense, which refers to an extension beyond the temporal limits of a single release. It denotes a continuous nominal 9-year deformation record that extends the 5–6-year observation span of any individual release by approximately 50–80%. (ii) From an analytical point-of-view, the HDRC formulation characterizes changes between successive deformation regimes, which avoids missing the partial response through a full-history hydro-deformation correlation analysis. (iii) From a geophysical perspective, the study evaluates these responses jointly in the vertical and horizontal components and examines their spatial organization, geological differentiation, and persistence across multiple GWL transitions. Furthermore, the novelty of this study lies in connecting multi-release EGMS harmonization directly with process-oriented deformation interpretation. Since the proposed methodology can accommodate new EGMS releases (which will be available in the future), it provides a transferable framework for the broader EGMS-user community and for future studies investigating other environmental or geophysical drivers of long-term deformation.

The remainder of this paper is structured as follows: Section 2 introduces the study area and datasets, encompassing multi-release EGMS Ortho products, groundwater levels, and geological records. Section 3 outlines the methodological framework, detailing the enhanced TAST, ULT DefTS reconstruction, and hydro-deformation response characterization. Section 4 evaluates the results, specifically highlighting alignment performance, spatiotemporal hydro-deformation dynamics, geological conditioning, and study limitations. Finally, Section 5 concludes with the principal findings and the broader implications of the proposed approach.

2. Materials

2.1. Area of Interest

The area of interest (AoI) covers wide sectors of the Como and Lecco Provinces, Lombardy Region, northern Italy (Figure 1a), extending across the transition between the Southern Alpine/Prealpine reliefs and the northern Po Plain. Several groundwater-level (GWL) monitoring stations are distributed within and around the study area and provide the hydrological observations considered in this study (see Section 2.3).

The AoI is characterized by a heterogeneous hydrogeological setting resulting from Alpine bedrock geology and Quaternary glacial, fluvioglacial, lacustrine, and alluvial processes. As shown in Figure 1b, the lower-relief sectors are extensively occupied by recent alluvial and terraced deposits, Late Pleistocene fluvioglacial gravels and sands, glacial–fluvial–lacustrine deposits, and morainic materials, whereas the surrounding reliefs expose carbonate, marly, clayey, and flysch-type bedrock units. Previous studies in the Como–Lecco area describe groundwater systems composed of shallow phreatic and locally deeper semi-confined or confined aquifers, with substantial spatial variability in sedimentary facies and hydraulic properties [32,33]. Such hydrogeological heterogeneity provides the

physical context for investigating spatial variations in the ground response to groundwater-level changes.

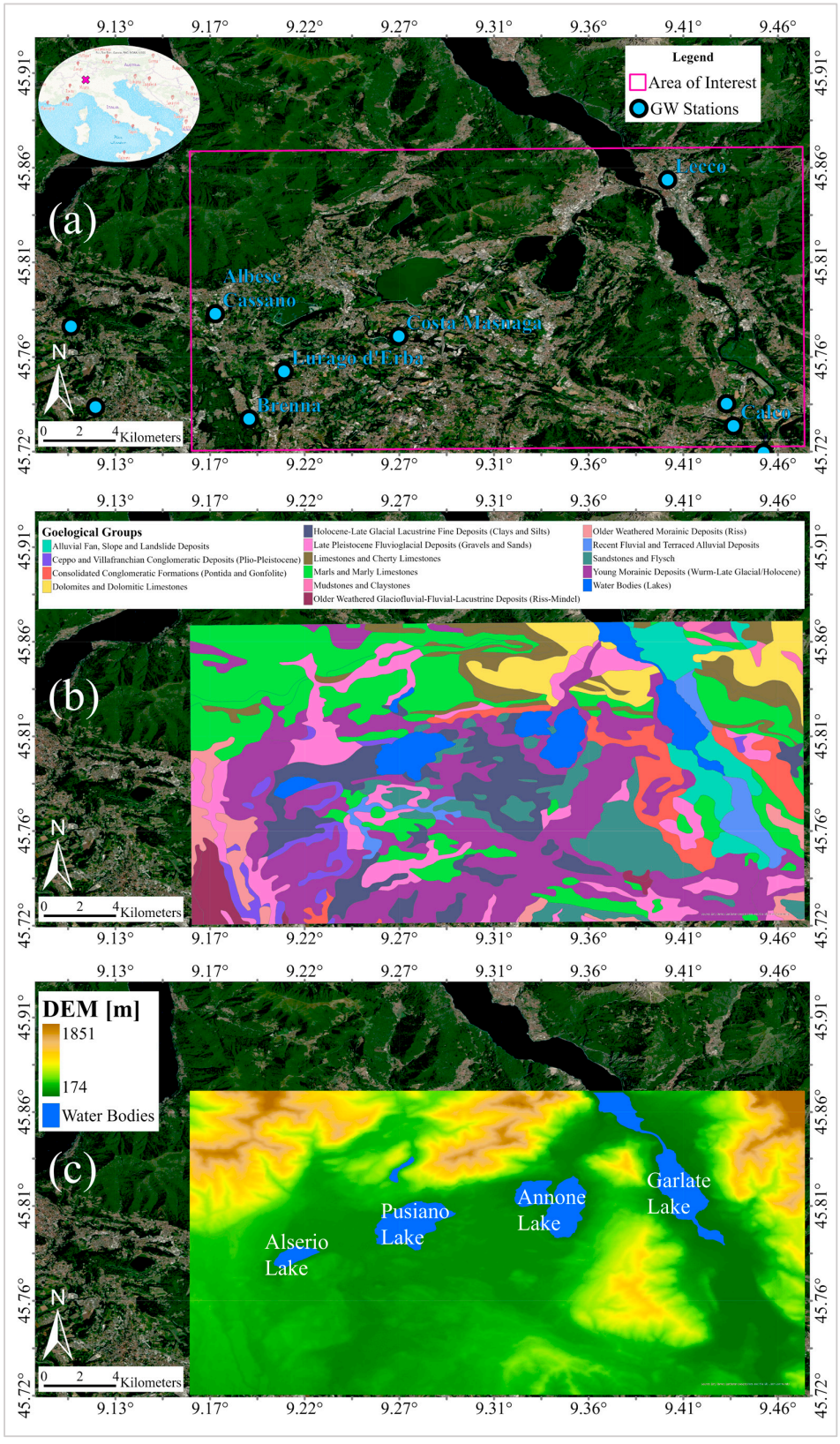

Figure 1. Overview of the study area in the Lecco–Como sector of northern Italy: (**a**) location of the area of interest (AoI) and groundwater-level monitoring stations; (**b**) spatial distribution of the geological groups; and (**c**) digital elevation model (DEM) and major water bodies within the AoI.

Topography is also highly variable across the AoI, with elevations ranging from approximately 174 to 1851 m a.s.l. (Figure 1c). Low-elevation sedimentary plains and lake basins are surrounded by steep Prealpine reliefs, while several major water bodies, including Alserio, Pusiano, Annone, and the Garlate Lakes, occur within the investigated domain.

2.2. InSAR Data: EGMS Ortho Products

EGMS, operated within the Copernicus Land Monitoring Service (CLMS), provides free-access and standardized ground-deformation measurements with Pan-European coverage. The service is based on MT-InSAR processing of Sentinel-1 SAR imagery and provides DefTS and deformation data for distributed MPs [4,34]. The spatial representation and temporal sampling of the data depend on the EGMS product level, which comprises Basic (L2a), Calibrated (L2b), and Ortho (L3) products.

Basic (*L2a*) products represent the native MT-InSAR measurements and are provided independently for ascending and descending Sentinel-1 acquisition geometries. Each dataset approximately follows the original Sentinel-1 burst segmentation and contains DefTS along the satellite line-of-sight (LoS). The MPs are distributed according to the radar observations and therefore do not form a regular geographic grid. Each L2a dataset is referred to a local reference point, meaning that its displacement measurements are relative within the corresponding processing unit.

Calibrated (*L2b*) products retain the same LoS representation and ascending/descending separation but are referenced to a model derived from the European GNSS network. This calibration removes the dependence on individual local reference points and anchors the measurements to a common Earth-centered geodetic reference frame, enabling comparison among spatially adjacent EGMS datasets.

Ortho (*L3*) products are derived from the calibrated ascending and descending datasets. Measurements from both acquisition geometries are aggregated onto a common 100 × 100 m grid, considering cells for which sufficient observations from both geometries are available. Their LoS measurements are subsequently decomposed into vertical Up–Down (U-D) and horizontal East–West (E-W) displacement components, while a north–south (N-S) InSAR component is not independently provided because of the limited sensitivity of the Sentinel-1 acquisition geometry in that direction. The resulting L3 DefTS are referenced to the same GNSS-derived geodetic framework and are provided with a nominal 6-day temporal sampling. The products are distributed in 100 × 100 km ETRS89-LAEA tiles (EPSG:3035) and each Ortho MP is characterized by a unique "pid" identifier. For grid cells available in multiple releases, this identifier allows the corresponding MPs to be consistently matched between datasets.

These EGMS products are planned to be periodically updated to extend ground-motion monitoring through successive temporal windows. At the time of this study, four release datasets were provided, covering January 2016–December 2021 (R1), January 2018–December 2022 (R2), January 2019–December 2023 (R3), and January 2020–December 2024 (R4), with their main characteristics summarized in Table 1. From R2 onwards, the service follows a five-year moving-window update strategy. In this study, the four releases (i.e., R1 to R4) of the E42N25 Ortho tile (covering the whole AoI) were acquired [35] and processed for both the U-D and E-W components. These partially overlapping multi-release DefTS, with a nominal total span of 9 years (January 2016–December 2024), constitute the InSAR dataset subsequently used to construct the ULT deformation records (i.e., approximately 50–80% beyond the temporal window of an individual release).

Table 1. Spatial and temporal characteristics of multi-release European Ground Motion Service (EGMS) Ortho datasets.

	Release			
Properties	**R1**	**R2**	**R3**	**R4**
Start Date	January 2016	January 2018	January 2019	January 2020
End Date	December 2021	December 2022	December 2023	December 2024
Num. of time points (temporal coverage)	363 (6 years)	302 (5 years)	302 (5 years)	303 (5 years)
Nominal resolution (spatial, temporal)	(100 m, 6-day)	(100 m, 6-day)	(100 m, 6-day)	(100 m, 6-day)

2.3. Groundwater-Level Observations

Groundwater-level (GWL) time series were retrieved from the monitoring network of Lombardy's Regional Agency for Environmental Protection (ARPA) [36] for the Como and Lecco Provinces. The available groundwater-monitoring stations across the AoI are shown in Figure 1a. Among them, stations providing sufficiently representative temporal coverage over the EGMS total observation period (January 2016–December 2024) were selected to characterize the regional groundwater regime. The selected stations are Albese con Cassano, Brenna, Calco, Costa Masnaga, Lecco, and Lurago d'Erba.

The original GWL observations, provided with respect to the ground surface local reference, were re-referenced w.r.t. the first available measurement at the beginning of 2016 per each station. Accordingly, the resulting time series represent relative GWL variations w.r.t. to their respective initial conditions, as shown in Figure 2. Despite local differences in amplitude and short-term variability, the selected stations exhibit a broadly coherent multi-year variation pattern over the EGMS observation period. The regional hydrological regime highlighted in Figure 2 is subsequently used to define the temporal segmentation of the ULT DefTS into partial deformation periods, as described in Section 3.4.1.

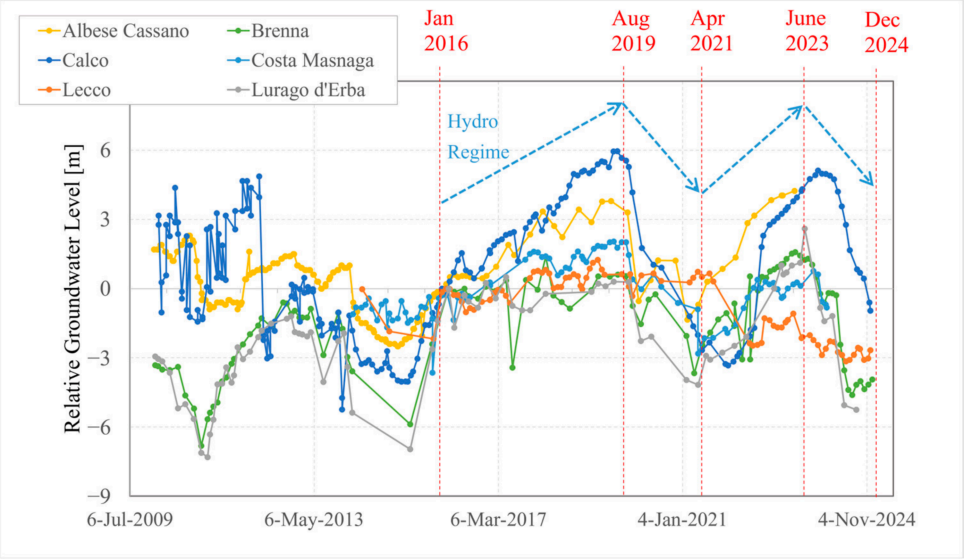

Figure 2. Groundwater-level (GWL) time series for the indicated stations in Figure 1a, and indicated variation regime from January 2016 to December 2024.

2.4. Geological Data

Geological information used in this study was obtained from the Geoportal of the Lombardy Region [37]. The dataset represents the regional distribution of lithological units, faults, and thrusts at 1:250,000 scale and was derived from the digitization of the geological map produced by Regione Lombardia administration in collaboration with the Department of Earth Sciences of the University of Milan in 1990.

The original geological polygons, falling into the AoI, comprised 32 distinct mapped units (including lacustrine areas). To reduce this categorical complexity and obtain a classification more suitable for the spatial analyses performed in this study, the original units were reclassified into 14 geological groups plus water bodies (lakes), as shown in Figure 1b. The regrouping was primarily based on similarities in dominant lithology, depositional origin, degree of consolidation, and geological age/weathering where these distinctions were considered relevant.

Notably, unconsolidated Quaternary deposits were differentiated into major alluvial, fluvioglacial, lacustrine, and morainic groups, while bedrock formations were aggregated into broader lithological classes such as limestones, dolomitic rocks, marls, mudstones/claystones, sandstones/flysch, and conglomeratic formations. This regrouping allows for preserving the main geological contrasts that are potentially relevant to groundwater circulation and ground deformation response, while avoiding an excessively fragmented categorical representation of the AoI.

3. Methods

3.1. Overview of the Adopted Workflow

The methodological workflow adopted in this study is summarized in Figure 3 and follows the research questions introduced in Section 1. First, the multi-release EGMS Ortho datasets are spatially organized, and their cross-release availability is assessed to establish the observational basis for ULT deformation monitoring. The overlapping DefTS are then harmonized through the enhanced TAST procedure, and the pairwise transformations are cumulatively propagated to construct temporally consistent ULT DefTS within a common reference frame. Subsequently, the ULT records are segmented according to the principal regional GWL turning points (TPs), and partial deformation trends are compared across successive hydro-regime periods through the HDRC metric to characterize the sign, magnitude, and spatial organization of the deformation response. Finally, the resulting HDRC patterns are stratified by geological group and statistically evaluated to determine whether the observed responses are systematically conditioned by geological setting and whether these relationships persist across successive GWL transitions.

3.2. Statistical Temporal Alignment

The initial concept of TAST was introduced by Eskandari and Scaioni [21] for the temporal harmonization of DefTS derived from different releases of the EGMS Ortho products. Considering the DefTS of release i as the reference time series TS_{ref} and that of release j as the time series to be aligned, TS_{alg}, both corresponding to the same MP, TAST exploits the period of temporal overlap between both releases (TS^{ovr}_{ref} and TS^{ovr}_{alg}) to estimate the required alignment parameters. In its original formulation, a transformation combining a vertical translation Γ with a linear scaling term θ was applied to TS^{ovr}_{alg}.

The optimal transformation was identified by maximizing the statistical similarity between TS^{ovr}_{ref} and TS^{ovr}_{alg}, quantified using the p-value of the non-parametric two-sample Anderson–Darling (AD) test, namely p_{AD}. Accordingly, the optimization problem was formulated by minimizing $[1 - p_{AD}]$. Since the AD test evaluates the Null Hypothesis that

the compared samples originate from the same underlying distribution, maximization of its *p*-value was used as a statistical criterion for identifying the alignment configuration.

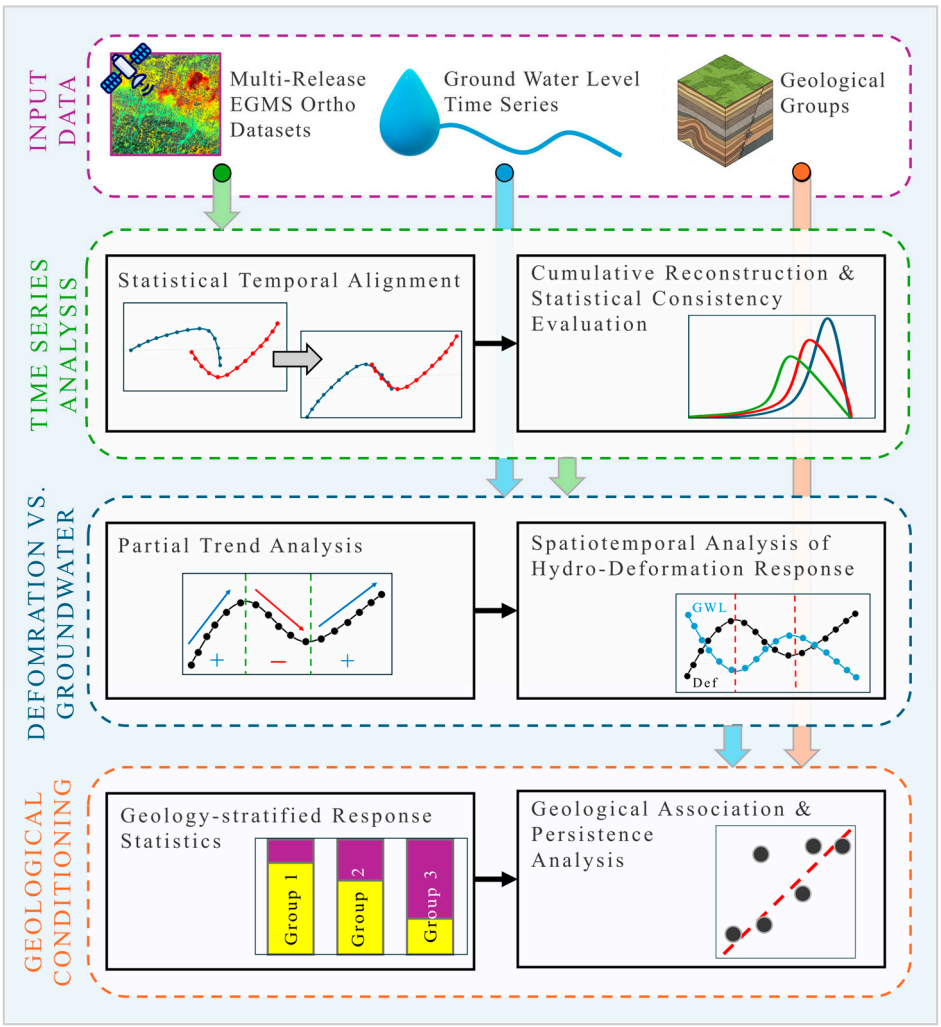

Figure 3. Methodological workflow from successive EGMS Ortho releases to hydro-geological interpretation of deformation.

3.2.1. Technical Obstacles

Three methodological limitations become relevant when the objective is to generate physically consistent ULT DefTS from multiple EGMS releases.

First, the linear scaling component of the original transformation can modify the internal deformation structure of an individual EGMS release. Each release originates from a complete and internally consistent MT-InSAR processing campaign; therefore, the relative deformation evolution estimated within that processing should be preserved during inter-release transformation. A multiplicative or deformation-amplitude scaling can significantly modify the relative magnitude of displacement variations within TS_{alg}, including the amplitudes of nonlinear or transient deformation components.

Second, a two-sample *p*-value alone does not provide a sufficient measure of temporal correspondence. The AD test compares the empirical distributions of two samples but does not consider the chronological ordering or epoch-to-epoch correspondence of their observations. Consequently, two overlapping DefTS may exhibit similar ranges and empirical distributions while having substantially different, or even opposite, temporal evolution. An illustrative extreme case consists of two approximately monotonic series span-

ning comparable deformation ranges but evolving in opposite directions during the overlap, thereby forming an X-shaped configuration (see Section 4.2.1). Despite their evident temporal inconsistency, their marginal distributions can remain very similar and consequently yield a relatively high two-sample p-value. Moreover, because two-sample statistics are constructed from empirical distribution functions and sample ranks, the resulting objective surface may contain relatively flat regions and abrupt variations as transformation parameters change. Such behavior can reduce the identifiability of a unique optimum and increase the possibility of convergence to suboptimal configurations.

Third, the use of the AD test itself introduces additional limitations when its p-value is employed as an optimization criterion. The AD statistic is specifically designed to assign greater weight to discrepancies occurring towards the tails of the compared distributions [38]. Considering this for the deformation measurements, a relatively small number of extreme deformation observations may exert a disproportionate influence on the statistical similarity measure compared with observations representing the central part of the overlapping series. Furthermore, computation of the AD p-value commonly relies on interpolation from a finite set of tabulated critical values. Such truncation becomes particularly restrictive when the p-value is used directly as an optimization objective, since different transformation configurations can receive the same upper-bound p-value, producing plateau regions in the objective space and reducing the ability of the optimizer to discriminate among increasingly similar configurations.

3.2.2. Enhanced TAST

To address those technical limitations while retaining the statistical–distributional basis of TAST, an enhanced TAST formulation is proposed in this study. Recalling the to-be-aligned DefTS in the overlapping period TS_{alg}^{ovr}, the transformation function is defined as

$$\overline{\overline{TS_{alg}^{ovr}}}(t) = TS_{alg}^{ovr}(t) + \Gamma + \vartheta(t - t_0) \tag{1}$$

where Γ and ϑ are the transformation parameters, referred to as *Translation* [mm] and *Velocity Correction* [mm/y], respectively. The variable t (in years) represents the observation epoch and t_0 is the reference epoch, defined as the beginning of the temporal overlap between both releases.

The optimal transformation parameters are estimated by minimizing the following composite objective function:

$$\min_{\{\Gamma,\vartheta\}}\left[\left(1 - p_{CvM}\left(TS_{ref}^{ovr}, \overline{\overline{TS_{alg}^{ovr}}}\right)\right) + RMSE\left(TS_{ref}^{ovr}, \overline{\overline{TS_{alg}^{ovr}}}\right)/R_0\right] \tag{2}$$

where p_{CvM} denotes the p-value of the two-sample non-parametric Cramér-von Mises (CvM) test and *RMSE* (Root Mean Square Error) quantifies the pointwise discrepancy between the reference and transformed DefTS over their common temporal interval. Both terms are expressed in dimensionless form by normalizing RMSE using a fixed reference scale $R_0 = 1$ mm. In fact, this fixed reference was selected because normalizing *RMSE* by variables such as deformation range, standard deviation, maximum RMSE, etc., may introduce a data-dependent scaling factor that could change from MP to MP and release pair. In the current form, equal weights are assigned to the distributional and temporal terms. The fixed 1 mm scale provides dimensional normalization while defining a common, non-data-dependent reference scale for the relative contribution of the RMSE term. The objective-function value itself has no physical interpretation and is not subsequently used as a measure of alignment quality. Its purpose is exclusively to identify transformation parameters satisfying both distributional and epoch-wise temporal agreement. Moreover, the additive formulation of the objective function was preferred because it prevents a near-zero value of one criterion

from masking poor agreement in the other, as may occur in a multiplicative formulation. Regarding the calculation of *RMSE*, where an isolated acquisition epoch is unavailable in one release but present in the other, the missing value can be reconstructed by spline interpolation using the temporally neighboring observations of the corresponding DefTS.

The adopted objective function formulation was further evaluated from two complementary perspectives. First, the additive combination of the distributional and temporal criteria was assessed against the corresponding single-criterion formulations, i.e., normalized *RMSE* alone and $1 - p_{CvM}$ alone, to verify the benefit of their joint consideration. Second, since the fixed reference scale R_0 controls the relative contribution of the *RMSE* term within the composite objective, sensitivity to this choice was additionally assessed using alternative R_0 values of 0.5 and 2 mm, respectively corresponding to an increase and decrease in the relative contribution of the temporal-agreement term. The resulting alignment parameters and post-alignment statistical consistency were compared with the $R_0 = 1$ mm reference solution (see Section 4.2.1).

The modifications introduced in the enhanced TAST formulation were specifically designed to address the limitations discussed in Section 3.2.1, described as follows:

- The multiplicative linear-scaling term of the original formulation is replaced by an additive linear velocity correction. The transformation in Equation (1) consists exclusively of a rigid vertical translation and a uniform linear-in-time correction, which avoids rescaling individual displacement observations or modifying the relative amplitudes of nonlinear deformation variations within a single EGMS processing campaign.
- Distributional similarity is complemented by an explicit measure of temporal correspondence. Both terms of Equation (2) play complementary roles: $\left(1 - p_{CvM}\left(TS_{ref}^{ovr}, \overline{\overline{TS_{alg}^{ovr}}}\right)\right)$ is used as a criterion penalizing evidence against distributional compatibility between the overlapping DefTS, while $RMSE\left(TS_{ref}^{ovr}, \overline{\overline{TS_{alg}^{ovr}}}\right)$ evaluates their epoch-wise deformation agreement, penalizing configurations in which corresponding observations remain separated despite having similar marginal distributions. Therefore, the composite objective requires the transformed DefTS to satisfy both distributional and temporal consistency simultaneously.
- The AD test adopted in the original TAST is replaced by the CvM test. Both statistical tests are non-parametric and evaluate whether two samples may originate from the same underlying distribution. However, CvM evaluates the integrated squared discrepancy between both empirical distribution functions over their complete range, which is considered more appropriate for the present alignment problem, where similarity across the overall deformation distribution is of primary interest rather than preferential sensitivity to its extreme values.

3.3. Ultra-Long-Term DefTS Construction and Multi-Release Consistency Assessment

Following the Enhanced TAST formulation, the procedure was extended to the multi-release EGMS DefTS to construct a temporally referenced ultra-long-term DefTS. The procedure is independently applied to each MP and deformation direction $d \in \{\text{U-D, E-W}\}$. For two consecutive available releases, the older release j, hereafter referred to as the source release, is aligned onto the next available recent release i, considered as the target release. Accordingly,

$$\begin{cases} TS_{ref}^{ovr} = DefTS_i^d \\ TS_{alg}^{ovr} = DefTS_j^d \end{cases} \tag{3}$$

with

$$j = \max\{k \in A^d : k < i\} \tag{4}$$

where A^d denotes the set of available EGMS releases for the considered MP and direction. This definition ensures that, when an intermediate release is unavailable, the source release is aligned directly onto the next available release. For example, when all four releases are available, independent pairwise TAST estimations are performed as R1→R2, R2→R3, R3→R4. The resulting pairwise transformation parameters are $\{\Gamma_{12},\vartheta_{12}\}$, $\{\Gamma_{23},\vartheta_{23}\}$, and $\{\Gamma_{34},\vartheta_{34}\}$, respectively.

The logic implemented in the current alignment workflow is that each pairwise transformation is estimated independently using the raw DefTS of the two releases involved, prior to any cumulative transformation. The most recent available release is subsequently adopted as the global reference release. Thus, R4 is used as the global reference whenever available, since it represents the most recent EGMS processing period and provides the temporal endpoint of the reconstructed ULT DefTS. Keeping this release unchanged also avoids introducing unnecessary corrections into the most recent deformation observations.

In practice, the pairwise transformations are then cumulatively composed to map all preceding releases into this common global reference frame. Defining the *ji* pairwise correction as follows:

$$C_{j\to i}(t) = \Gamma_{ji} + \vartheta_{ji}(t - t_{0,ji}), \tag{5}$$

The globally referenced DefTS of a release r with global reference release g can be expressed as

$$\widehat{DefTS}_r^d(t) = DefTS_r^d(t) + \sum_{(j\to i)\in P_{r\to g}} C_{j\to i}(t), \tag{6}$$

where $P_{r\to g}$ represents the sequence of pairwise transformations connecting release r to the global reference g. Since each correction is itself linear in time, the complete transformation chain can equivalently be represented by a single cumulative translation $\hat{\Gamma}_{ji}$ and cumulative velocity correction $\hat{\vartheta}_{ji}$. For an arbitrary pivot epoch τ, these cumulative (global) transformation parameters are expressed as

$$\hat{\vartheta}_{r\to g} = \sum_{(j\to i)\in P_{r\to g}} \vartheta_{ji}, \tag{7}$$

and

$$\hat{\Gamma}_{r\to g} = \sum_{(j\to i)\in P_{r\to g}} \left[\Gamma_{ji} + \vartheta_{ji}\left(\tau - t_{0,ji}\right)\right], \tag{8}$$

and are used to transfer each older release through its complete transformation chain into the newest-release reference frame. Additionally, alignment sensitivity and path-dependent discrepancies are assessed by comparing the cumulative R1→R4 and R2→R4 transformations with separately estimated direct-to-R4 transformations. The operation is performed w.r.t. to the pivot epoch τ for the sake of comparability. The statistics and parameter-difference distributions provided by this analysis can offer an empirical characterization of path sensitivity.

Following global referencing, a single ULT DefTS is obtained by taking the median deformation value at each exact observation epoch across all globally referenced releases available at that epoch:

$$\mathrm{DefTS}_{\mathrm{ULT}}^d(t) = median\left\{\widehat{DefTS}_r^d(t) \ : r \ \in A_t^d \right\} \tag{9}$$

where A_t^d contains the globally referenced releases providing an observation exactly at epoch t. Hence, overlapping releases jointly contribute to the ULT estimate, whereas epochs covered by only one release retain the deformation value from that transformed release.

In addition to the ULT DefTS, the final pairwise alignment results are used to quantify the post-alignment inter-release consistency. For a single deformation component of

an arbitrary MP, the Statistical Consistency Index (SCI) for each overlapping release pair is defined as

$$\mathrm{SCI}_{j\to i} = \left[1 + \frac{W_1\left(TS^{ovr}_{ref}, \overline{\overline{TS^{ovr}_{alg}}}\right)}{IQR\left(\left[TS^{ovr}_{ref}, \overline{\overline{TS^{ovr}_{alg}}}\right]\right)}\right]^{-1} \quad (10)$$

where W_1 denotes the first Wasserstein distance between the aligned overlapping DefTS, normalized by the interquartile range (IQR) of their concatenated observations. This normalization makes the discrepancy dimensionless and scales it according to the intrinsic deformation variability of the compared pair, without requiring information from other MPs or release pairs. The reciprocal transformation bounds SCI within $(0, 1]$, with unity corresponding to coincident empirical distributions, and progressively smaller values indicating greater residual distributional disagreement. The IQR-based scaling also reduces sensitivity to isolated extreme observations, while the Wasserstein distance accounts for differences across the complete empirical distributions without relying on hypothesis-test significance. This metric provides a quantitative diagnostic of the internal statistical consistency between overlapping releases after alignment. Nevertheless, it should not be interpreted as a measure of absolute deformation accuracy, which would require validation against independent observations.

3.4. GWL-Deformation Response Analysis

To interpret the deformation dynamics revealed by the constructed ULT DefTS and to assess their ability to capture real-world temporal changes, the spatiotemporal modifications of the deformation regime associated with variations in GWL were investigated.

3.4.1. Segmentation of the Monitoring Period

The relative GWL time series shown in Figure 2 were used to characterize the temporal evolution of the groundwater regime. A direct correlation between each ULT DefTS and a locally representative GWL series, obtained either through spatiotemporal interpolation or selection of the nearest monitoring station, was not adopted for two main reasons: (i) the GWL–deformation relationship is potentially non-stationary over the full monitoring interval; periods characterized by weak or different responses could therefore mask meaningful correlations occurring within individual hydro-regimes, and (ii) the GWL records exhibit heterogeneous sampling frequencies, temporal gaps, and occasional anomalous or out-of-range observations, making continuous interpolation and subsequent pointwise correlation comparatively uncertain and strongly dependent on preprocessing assumptions.

The principal hydro-regime transitions are clearly recognizable from the regional evolution of the relative GWL records shown in Figure 2. Nevertheless, to avoid relying exclusively on graphical interpretation and to provide an objective and reproducible basis for temporal segmentation, the TP locations were assessed through a dedicated TP detection procedure [39] applied to the regional standardized GWL behavior, as detailed in Appendix B. The analysis identified three dominant TP intervals centered on August 2019, April 2021, and June 2023, which were adopted as TP1, TP2, and TP3, respectively. Together with the nominal beginning and end of the ULT monitoring interval, January 2016 and December 2024, respectively, these turning points divide the observation period into four hydro-regime periods (P1–P4), as shown in Figure 2. These periods provide the temporal framework for evaluating modifications in the deformation regime associated with successive changes in GWL behavior.

To assess the influence of the adopted TP dates on the subsequent analyses and to provide an explicit assessment of the robustness of the downstream interpretation to uncertainty in the exact TP locations, a sensitivity experiment was performed by independently

shifting each TP by −6, −3, +3, and +6 months while retaining the remaining TPs at their reference locations. For each perturbation, the adjacent partial deformation velocities and HDRC values were recomputed, followed by reassessment of HDRC agreement, spatial autocorrelation, and geological conditioning. The complete sensitivity statistics are provided in Appendix C.

3.4.2. Partial Trend Analysis

Accordingly, each ULT DefTS was partitioned into the four hydro-regime periods P1–P4. For each partial DefTS containing at least 60 valid observation epochs, the deformation evolution was modelled as the combination of a first-order polynomial trend and a sinusoidal component:

$$D(t) = [a_0 + a_1\, t] + [s_1 \sin(2\pi t) + s_2 \cos(2\pi t)] \tag{11}$$

where t is expressed in years, a_0 is the intercept, a_1 represents the underlying linear deformation velocity, and s_1 and s_2 describe the annual periodic component. The harmonic terms were included to reduce the influence of seasonal deformation variations on the estimation of the underlying linear trend. Here, the resulting slopes a_1 were retained as the deformation velocities for the four periods, hereafter denoted as DefV_{P1} to DefV_{P4}. The threshold of 60 epochs was adopted for two reasons: (i) with the nominal 6-day sampling, 60 epochs correspond to approximately one year (a full annual cycle) which is required to reliably separate the annual harmonic component from the linear trend; (ii) it leaves a large number of residual degrees of freedom for the four parameters of Equation (11), ensuring a well-conditioned least-squares estimation. Given that the shortest hydro-regime periods (P2 and P4) span approximately 18–20 months (~90–100 epochs), this criterion only excludes MPs with substantial data gaps within a period.

It is worth mentioning that the MPs for which R4 was unavailable, and for which the ULT DefTS was consequently referenced to an earlier available release, were excluded to avoid mixing deformation records expressed within different global release-reference frames and to ensure consistency of the subsequent spatial comparison.

3.4.3. Hydro-Deformation Regime Concordance Definition

Following the derivation of the partial deformation velocities, changes in deformation behavior across consecutive hydro-regime periods were related to the corresponding GWL turning points. As illustrated in Figure 2, TP1 and TP3 represent transitions from increasing to decreasing (i.e., *concave*) GWL conditions, whereas TP2 represents the opposite transition from decreasing to increasing (i.e., *convex*) GWL conditions. For each turning point TPk with k ∈ {1,2,3}, located between two consecutive periods Pm and Pn, the differential velocity is first defined as

$$\Delta\mathrm{DefV}^{d}_{\mathrm{TP}k} = \mathrm{DefV}^{d}_{\mathrm{P}n} - \mathrm{DefV}^{d}_{\mathrm{P}m}, \tag{12}$$

for direction $d \in$ {U-D, E-W}. A hydro-regime sign coefficient is then introduced as

$$H_{\mathrm{TP}k} = \begin{cases} -1 \text{ for } \mathrm{GWL}_{concave}, \\ +1 \text{ for } \mathrm{GWL}_{convex}. \end{cases} \tag{13}$$

Accordingly, the Hydro-Deformation Regime Concordance (HDRC) is defined as

$$\mathrm{HDRC}^{d}_{\mathrm{TP}k} = H_{\mathrm{TP}k} \,.\, \Delta\mathrm{DefV}^{d}_{\mathrm{TP}k} \tag{14}$$

which is expressed in [mm/year] units. Its magnitude represents the absolute change in deformation velocity across the corresponding TP, whereas its sign describes whether the

transition of deformation regime follows or opposes the curvature of the GWL regime. Therefore, HDRC is a regime-transition concordance metric: it quantifies the magnitude and direction of deformation-velocity changes relative to the direction of regional GWL transitions. Consequently, larger absolute HDRC values do not necessarily represent stronger hydro-mechanical coupling, but they indicate larger deformation velocity modifications.

For the U-D component, positive and negative velocities conventionally represent uplift and subsidence, respectively. At TP1 and TP3 with concave GWL behavior, positive HDRC corresponds to concavity in deformation, including: (i) transitions from uplift to subsidence; (ii) uplift to lower-rate uplift; or (iii) subsidence to higher-rate subsidence. At the convex GWL transition of TP2, positive HDRC corresponds to convexity in deformation, including: (i) subsidence-to-uplift transitions; (ii) subsidence to lower-rate subsidence; or (iii) uplift to higher-rate uplift. Negative HDRC values indicate the opposite, or anti-phase, response.

For the E-W component, the same mathematical definition is retained, although its physical interpretation differs because, based on convention, positive and negative velocities represent eastwards and westwards motion, instead of uplift and subsidence. Although groundwater-driven horizontal deformation may arise from hydraulic-gradient variations in different geological settings (e.g., sedimentary aquifers [40] and fractured carbonate rocks [41]), the E-W HDRC defined here does not identify a specific hydro-mechanical mechanism. Instead, it quantifies the directional concordance between changes in E-W deformation regime and the corresponding regional GWL transition. Consequently, positive HDRC at TP1 and TP3 denotes a decrease in E-W velocity, such as eastwards-to-westwards motion, eastwards motion at a reduced rate, or westwards motion at an increased rate. At TP2, positive HDRC denotes an increase in E-W velocity, including westwards-to-eastwards motion, reduced-rate westwards motion, or magnified eastwards motion. Negative values represent the opposite directional response.

Additionally, to quantify the estimation uncertainty associated with the partial deformation velocities and its propagation into HDRC, a regression-based uncertainty analysis was performed, conditional on the adopted ULT reconstruction, TP dates, and partial-trend model. Joint covariance estimates for the four period-wise deformation velocities (DefV) were obtained from the regression design matrices and residuals using a Bartlett temporal covariance kernel based on the actual observation-date separations. Letting h denote the temporal bandwidth, the kernel weight was defined as $K_{ij} = \max[\, 1 - |t_i - t_j|/h,\, 0]$ for observations at epochs t_i and t_j. A fixed bandwidth of $h = 60$ days was adopted for all MPs, hydro-regime periods, and both deformation components, corresponding to approximately ten nominal 6-day EGMS sampling intervals. This common, non-data-dependent bandwidth was selected to represent short-range temporal dependence while avoiding MP-specific covariance assumptions. Thus, observations separated by 60 days or more receive zero covariance weight. Instead of observation index, the calculation uses the actual elapsed time, thereby naturally accounting for irregular temporal spacing or missing acquisitions. As a sensitivity check, the uncertainty calculation was additionally repeated using bandwidths of 30 and 90 days, representing respectively shorter and longer temporal-dependence supports around the adopted value. Period-specific residual contributions were corrected for the four fitted regression parameters, while shared observations at period boundaries and cross-period covariance contributions were retained. Specifically, defining S as the matrix of slope-influence contributions scaled by the finite-sample factor $\sqrt{n/(n-4)}$, the joint velocity covariance was estimated as $\hat{\sum}_v = S^T\, K\, S$. For each TP$k$, the resulting joint velocity-covariance matrix was finally propagated through the linear HDRC contrasts to obtain HDRC variance as $\mathrm{I}_k^T \hat{\sum}_v \mathrm{I}_k$ and approximate pointwise 95% intervals defined as $\mathrm{HDRC}_{\mathrm{TP}k} \pm 1.96\sqrt{\mathrm{I}_k^T \hat{\sum}_v \mathrm{I}_k}$. Here, $\mathrm{I}_1 = [1,-1,0,0]^T$, $\mathrm{I}_2 = [0,-1,1,0]^T$, and $\mathrm{I}_3 = [0,0,1,-1]^T$ denote the HDRC contrast vectors for TP1–TP3, respectively.

3.5. Geological Conditioning

To investigate whether the spatial variability and magnitude of the deformation response to GWL variations are conditioned by the geological setting, the derived HDRC values were spatially associated with the geological groups defined in Section 2.4. Since the EGMS Ortho products are represented on a spatially regularized grid, a limited number of MPs geometrically fall within polygons classified as water bodies. These grid locations do not necessarily represent deformation measurements physically originating from the lake surface, since the corresponding Ortho observations are derived from neighboring land-based calibrated EGMS measurements during the product-generation procedure. Therefore, to prevent the artificial introduction of a water-body geological class into the subsequent conditioning analysis, the MPs intersecting mapped water bodies were reassigned to the nearest non-water geological group.

The HDRC observations belonging to each geological group were subsequently aggregated and statistically evaluated per TP. The distribution of HDRC magnitudes was evaluated within each geological group to characterize the differences in the intensity of the hydro-deformation response. In parallel, the percentages of MPs exhibiting positive and negative HDRC were computed per group and TP to identify the prevalence of concordant and discordant deformation-regime responses within the different geological settings.

Additionally, the association between geological group and HDRC sign was evaluated using the Cramér's V, which rescales a Pearson χ^2 statistic onto a standardized $[0, 1]$ range [42], as an effect-size measure. Then, the temporal persistence of these geological response patterns was assessed by comparing the group-wise positive/negative HDRC percentages among the three TPs. Finally, pairwise agreement between TPs was evaluated using Spearman's rank correlation coefficient, while the overall consistency of the geological-group rankings across all three TPs was assessed using Kendall's coefficient of concordance. This particularly helps to understand if geological groups exhibiting stronger concordant or discordant responses retain similar relative behavior across successive hydro-regime transitions.

4. Results and Discussion

4.1. EGMS Ortho Measurement Point Availability and Release Continuity

The EGMS Ortho products provided a dense and broadly consistent spatial sampling of the study area throughout the four considered releases. As shown in Figure 4, a total of 16,294, 17,135, 17,096, and 16,213 MPs were identified within the AoI for R1, R2, R3, and R4, respectively, corresponding to average densities of 41.28, 43.41, 43.31, and 41.07 MP/km^2. The relatively limited variation among the releases indicates that the regional observational support remained comparable throughout the investigated period, with the maximum difference between release-wise MP populations being approximately 5.7%. R2 and R3 exhibited particularly similar coverage, differing by only 39 MPs.

More importantly, for the construction of the ULT deformation dataset, most MPs showed substantial persistence across successive EGMS releases. Approximately 87% of the identified MPs were represented in all four releases (R1–R4), while about 92% occurred in at least three releases. This high degree of cross-release persistence is particularly favorable for multi-release temporal harmonization, which is adopted in this study. For most MPs, the complete sequence of overlapping releases is available for estimating the successive inter-release corrections and propagating the observations into a common temporal reference frame. At the same time, the presence of a smaller population of MPs with incomplete release availability supports the use of an MP-specific alignment strategy, in which the transformation sequence is determined according to the releases actually available for each location rather than restricting the analysis exclusively to the four-release intersection. This

allows the subsequent ULT deformation analysis to retain a high spatial sampling density and a high degree of temporal observational continuity.

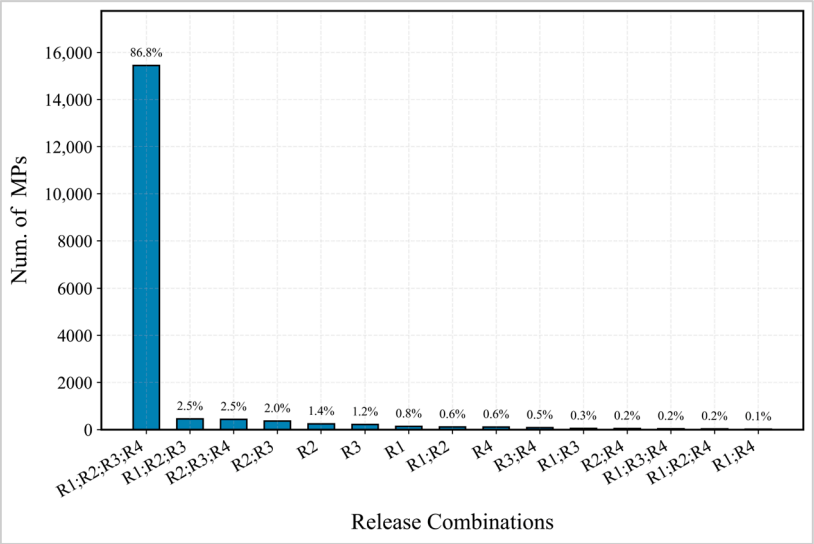

Figure 4. Distribution of EGMS Ortho measurement points according to their availability across the four releases within the Area of Interest (AoI).

4.2. Temporal Alignment Overview

The enhanced TAST procedure introduced at Section 3.2.2 was applied to all available adjacent release pairs per each MP within the AoI independently for the U-D and E-W deformation components. The pairwise transformations were first estimated between the corresponding raw releases and were subsequently composed to express all available releases within the reference frame of the most recent release. The globally aligned series were then used to construct the ULT DefTS according to the procedure described in Section 3.3.

Figure 5 illustrates the different stages of this procedure for a representative MP, while the corresponding transformation parameters are reported in Table 2. The raw multi-release DefTS (Figure 5a,d) show that R1, R2, and R3 generally preserve comparable deformation behavior within their respective overlapping periods, particularly in terms of the temporal variations and their broader trends. Nevertheless, agreement between independently processed releases is not maintained throughout the entire sequence. The most evident discrepancy occurs between R3 and R4, where a pronounced divergence develops from approximately late-2021 onwards in both deformation components. In the U-D direction, R3 progressively evolves towards subsidence while R4 remains at substantial uplift; an analogous but oppositely oriented trend discrepancy is apparent in the E-W component. Consequently, direct concatenation of the raw releases would introduce artificial long-term deformation trends that are related to inter-release inconsistency rather than to the underlying deformation evolution.

This discrepancy is reflected quantitatively by the estimated transformation parameters (Table 2). For the U-D component, the R3→R4 transformation requires a velocity correction of +5.656 mm/y, considerably larger than those obtained for R2→R3 (−0.438 mm/y) and R1→R2 (−0.107 mm/y). Similarly, the E-W component requires a large R3→R4 velocity correction of −6.234 mm/y, whereas the corrections associated with R2→R3 and R1→R2 are only +0.150 and −0.097 mm/y, respectively. The inter-release inconsistency affecting R3→R4 therefore dominates the long-term correction required for this MP. Because the individual transformations are propagated towards the R4 reference frame, these corrections accumulate for the earlier releases: the cumulative velocity correction reaches +5.111 mm/y

for R1 in the U-D direction and −6.180 mm/y in the E-W direction, accompanied by cumulative translations of −14.824 mm and +18.104 mm, respectively. These cumulative parameters should not be interpreted as independent R1→R4 estimates, but as the equivalent transformations resulting from composition of the successive pairwise corrections. After transformation to the common R4 reference frame (Figure 5b,e), the previously evident inter-release trend divergence is substantially reduced. In particular, the corrected R3 series follows the temporal evolution represented by R4 much more consistently within their overlapping interval, while the transformations applied farther backwards propagate this reference frame through R2 and R1.

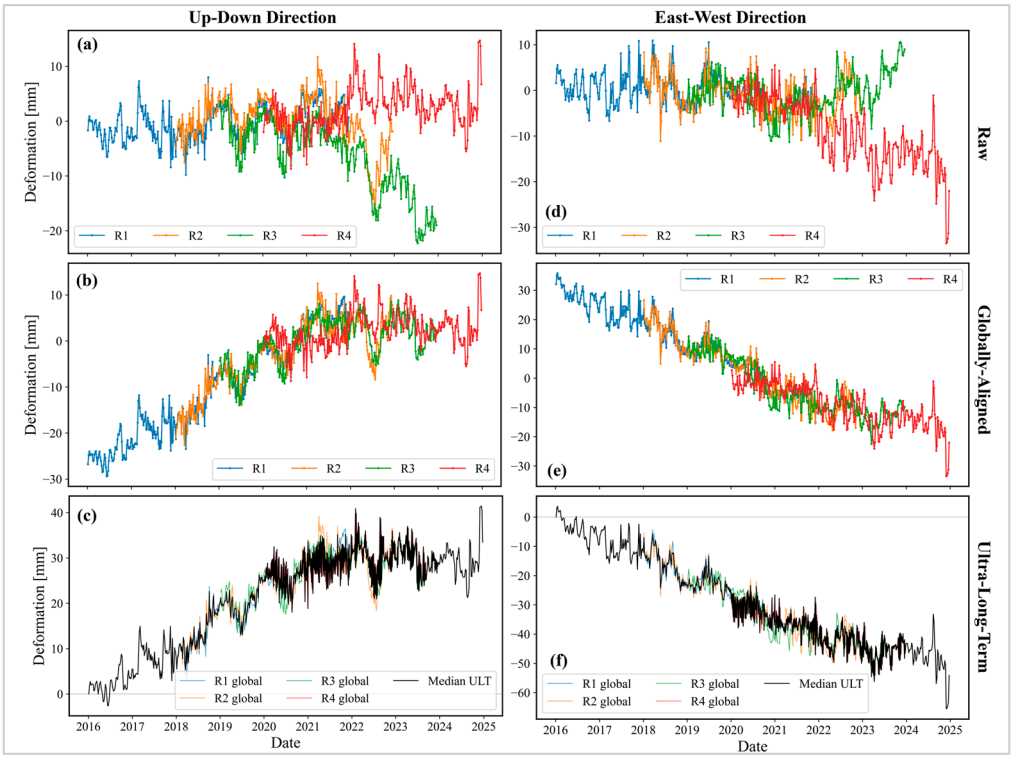

Figure 5. Example of multi-release temporal alignment for a representative measurement point (MP) (pid: 10UkUImEI4): raw deformation time series (DefTS) (**a**,**d**), globally aligned releases in the R4 reference frame (**b**,**e**), and reconstructed ultra-long-term (ULT) DefTS (**c**,**f**) for the Up–Down (U-D) and East–West (E-W) components, respectively.

Table 2. Output summary of the temporal alignment presented in Figure 5 (pid: 10UkUImEI4).

	Pair	Translation (Cumulative) [mm]	Velocity Correction (Cumulative) [mm/y]	*p*-Value
Up–Down Direction	R3→R4	−1.652 (−1.652)	+5.656 (+5.656)	0.100
	R2→R3	−3.586 (−10.890)	−0.438 (+5.218)	0.988
	R1→R2	+1.295 (−14.824)	−0.107 (+5.111)	0.977
East–West Direction	R3→R4	+5.788 (+5.788)	−6.234 (−6.234)	0.001
	R2→R3	+0.207 (+12.225)	+0.150 (−6.084)	0.707
	R1→R2	−0.218 (+18.104)	−0.097 (−6.180)	0.390

The example demonstrates that relatively small discrepancies between some release pairs can coexist with a much larger systematic trend difference in another pair, and that neglecting the latter would substantially distort the reconstructed ULT deformation history. In addition, an important feature of this example is that graphical alignment of the underly-

ing deformation evolution does not necessarily imply complete statistical equivalence of the overlapping observations. This is particularly evident for the E-W R3→R4 pair, for which the post-alignment CvM *p*-value remains only 0.001, despite the pronounced improvement in the consistency of the long-term trends. In comparison, the corresponding *p*-values for R2→R3 and R1→R2 are 0.707 and 0.390, while the U-D pairwise *p*-values are 0.100, 0.988, and 0.977 for R3→R4, R2→R3, and R1→R2, respectively. The low R3→R4 E-W *p*-value indicates that residual differences remain between the statistical distributions of both overlapping series, even after their systematic offset and trend discrepancy have been corrected. Therefore, a low final *p*-value does not demonstrate failure of the temporal alignment, since the optimum transformation may still substantially reconcile the underlying deformation trajectory while residual differences in noise, short-period variability, sampling, or the detailed distributions of both releases remain.

Figure 5c,f shows the ULT DefTS obtained after propagation of the transformations into the R4 reference frame and temporal assembly of the available releases. For visualization, the resulting ULT DefTS for both the U-D and E-W directions were re-referenced to their respective first observation (without altering the temporal evolution). The resulting series provides a continuous representation of the deformation dynamics extending from the beginning of the R1 (January 2016) to the end of the R4 (December 2024) observation period. Importantly, the observed dynamics emerge coherently across the boundaries of the original EGMS releases, illustrating the role of enhanced TAST in recovering deformation histories that would otherwise be strongly affected by release-dependent offsets and trend differences.

4.2.1. Justification on Objective Function Selection

Figure 6 provides a compact justification for choosing the combined objective function in the enhanced TAST procedure by comparing the alignment obtained using only temporal agreement with normalized $[RMSE]$, only distributional agreement $[1 - p_{CvM}]$, and their combination $[(1 - p_{CvM})$ + normalized $RMSE]$ (refer to Section 3.2.2). The example shows that the behavior of the optimization depends strongly on the characteristics of the overlapping release pair.

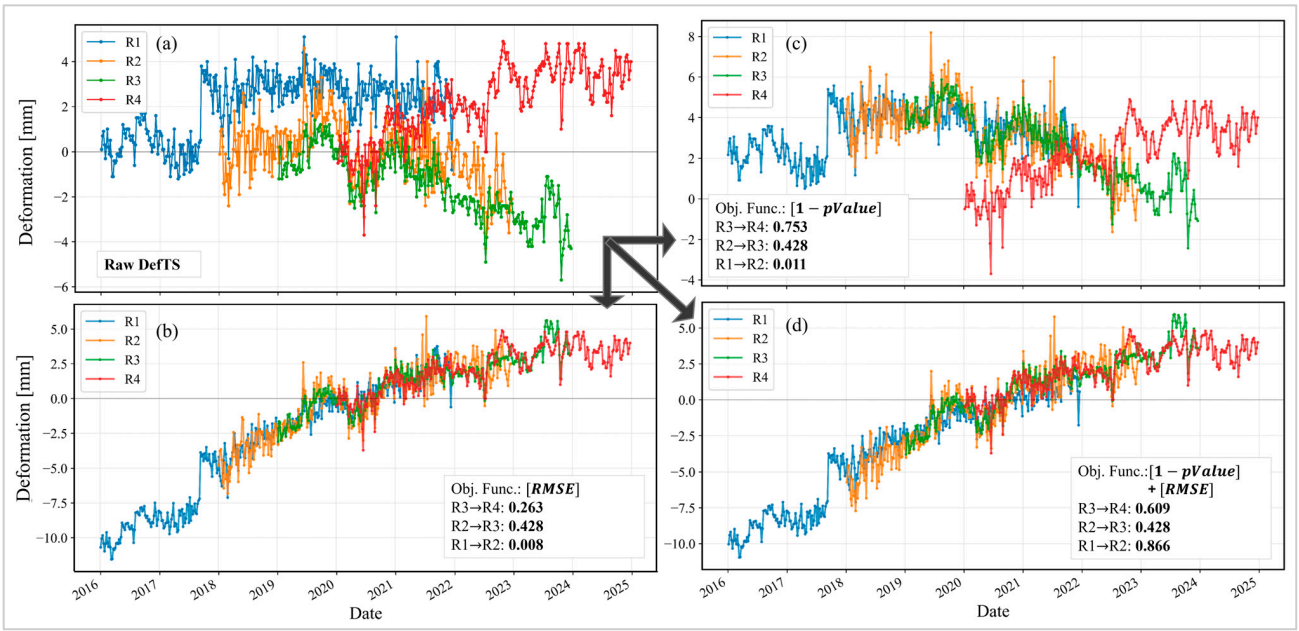

Figure 6. Comparison of the objective functions for temporal alignment: (**a**) raw DefTS, and alignment outputs using objective functions of (**b**) normalized *RMSE*, (**c**) $(1 - pValue)$, and (**d**) $(1 - pValue)$ + normalized *RMSE*. Values indicate post-alignment *p*-values for each release pair.

For R2→R3, all three formulations produce practically identical graphical alignment and the same post-alignment *p*-values, indicating that both releases are sufficiently consistent for the choice of the objective function to have negligible influence on the estimated transformation. A different behavior is observed for R1→R2. Here, optimizing either temporal or distributional agreement individually results in visually comparable alignments but very low *p*-values. In contrast, their combined consideration substantially increases the *p*-value, while retaining the temporal agreement of both series.

The R3→R4 pair illustrates the complementary limitation of optimizing the distributional agreement alone: although this criterion yields the highest *p*-value of 0.753, the resulting DefTSs remain inconsistent in their underlying temporal evolution, demonstrating the type of ambiguous solution discussed at Section 3.2.1. Conversely, *RMSE* alone recovers a much more plausible temporal alignment, but with a lower *p*-value of 0.263. The combined objective function provides a compromise between both requirements. It preserves the appropriate temporal evolution while increasing the post-alignment *p*-value to 0.609. These results support the use of a combined criterion in the enhanced TAST framework, since neither temporal nor distributional agreement alone is sufficient to provide robust transformation parameters under all inter-release conditions.

Furthermore, the robustness of the combined formulation to the relative weighting implied by R_0 (see Equation (2)) was assessed by repeating the pairwise alignment using $R_0 = 0.5$ and $R_0 = 2$ mm, and comparing the resulting parameter vectors with those obtained using the adopted $R_0 = 1$ mm reference case, reported in Table 3.

Table 3. Sensitivity of pairwise enhanced-TAST alignment parameters and post-alignment SCI to alternative RMSE scales, relative to the adopted $R_0 = 1$ mm reference case.

	Pair	R_0 Alt. [mm]	Translation		Velocity Correction		SCI				
			R^2 [ ]	StD [mm]	R^2 [ ]	StD [mm/y]	R^2 [ ]	StD [ ]	Impr. [%]	Wors. [%]	Unch. [%]
Up-Down Direction	R1→R2	0.5	0.998	0.099	0.986	0.050	0.988	0.005	40.748	42.639	16.613
		2	0.999	0.053	0.996	0.027	0.994	0.004	42.636	40.078	17.287
	R2→R3	0.5	0.998	0.068	0.990	0.033	0.992	0.005	44.893	36.118	18.989
		2	0.999	0.047	0.995	0.023	0.994	0.004	45.716	34.610	19.674
	R3→R4	0.5	0.998	0.065	0.991	0.032	0.993	0.004	46.419	33.646	19.935
		2	0.999	0.033	0.998	0.014	0.997	0.003	46.415	33.200	20.385
East-West Direction	R1→R2	0.5	0.997	0.110	0.985	0.057	0.981	0.005	43.877	37.709	18.414
		2	0.999	0.068	0.995	0.034	0.987	0.004	45.369	35.433	19.197
	R2→R3	0.5	0.996	0.097	0.986	0.047	0.986	0.005	44.255	37.256	18.488
		2	0.998	0.080	0.990	0.039	0.988	0.005	46.117	34.883	18.999
	R3→R4	0.5	0.993	0.114	0.986	0.057	0.983	0.004	45.652	41.436	12.912
		2	0.998	0.068	0.995	0.033	0.986	0.004	46.949	39.373	13.678

[R_0 Alt.: alternative RMSE normalizer; R^2: coefficient of determination; StD: standard deviation; Impr.: percentage of improvement; Wors.: percentage of decay; Unch.: percentage of unchanged.]

The estimated transformations remain highly stable across these variations in the RMSE normalization. For Translation, the coefficients of determination R^2 with respect to the reference solution are all greater than 0.99, with standard deviations of the differences not exceeding 0.114 mm. Velocity Correction shows similarly strong agreement, with corresponding standard deviations not exceeding 0.057 mm/y, indicating only small dispersion relative to the reference solutions. The independently calculated SCI is similarly stable, with $R^2 > 0.98$ and standard deviations of the differences not exceeding 0.005. Individual MPs may exhibit slightly improved or reduced SCI under alternative normalizations, which

indicates that no meaningful systematic improvement in post-alignment consistency was observed. These results demonstrate that the principal enhanced-TAST alignment solutions are insensitive to the modification of the RMSE reference scale and support $R_0 = 1$ mm as a stable fixed reference. It should be noted that the stability observed within $R_0 = 0.5$–2 mm does not imply numerical dominance of the RMSE term, since the single-criterion comparisons in Figure 6 demonstrate that inclusion of the CvM term can modify the optimized solution under challenging inter-release conditions.

4.2.2. Distribution of Velocity Correction Values

The transformation function adopted in the enhanced TAST procedure contains two parameters: a translation (Γ) and a velocity correction (ϑ). The translation mainly accommodates differences in deformation level between releases, including datum-related offsets and the effect of the selected temporal reference of the transformation. In contrast, the velocity correction parameter directly represents the difference in deformation trend between both releases over their overlapping period. The latter is therefore of greater relevance for ULT DefTS reconstruction, since overlapping EGMS Ortho releases, being calibrated within the GNSS-derived reference frame, would ideally be expected to exhibit mutually consistent deformation trends. Accordingly, the following analysis focuses on the spatial and statistical distribution of the estimated velocity corrections.

Figure 7 shows the spatial distribution of the velocity corrections obtained for the three consecutive alignment campaigns, R1→R2, R2→R3, and R3→R4, separately for the U-D and E-W components (the color scale is clamped to $[-1, +1]$ mm/y to preserve comparability and enhance visualization of the dominant regional spatial patterns). Although locally scattered MPs with different ϑ magnitudes are present, the maps reveal spatially coherent patterns extending over substantial portions of the AoI. This spatial organization indicates that the estimated ϑ may reflect systematic inter-release inconsistencies in the deformation trends of the EGMS Ortho products.

For the U-D component (Figure 7a–c), R1→R2 is characterized predominantly by negative ϑ values, with particularly coherent patterns extending from the surroundings of Garlate Lake towards the southeastern sector of the AoI and in the area north of Annone Lake (Valmadrera town). The R2→R3 corrections are generally smaller and more balanced, with predominantly negative values along the northern strip and near-zero to slightly positive ϑ values toward the southern sector. R3→R4 exhibits comparatively moderate corrections over much of the AoI, although coherent positive clusters are distinguishable around Garlate Lake, in the western part of Valmadrera town, and around north of Alserio Lake (center of Erba town).

A different spatial behavior is observed for the E-W component (Figure 7d–f). Relatively large corrections occur particularly within the mountainous and high-relief areas surrounding the more densely covered lowland sectors, with predominantly negative and positive patterns for R1→R2 and R2→R3, respectively. The most pronounced regional behavior is observed for R3→R4, where positive velocity corrections dominate almost the entire AoI within the displayed range. Such widespread spatial coherence indicates a regional-scale systematic trend mismatch between both releases. It is worth mentioning that no clear correspondence was observed between the U-D and E-W velocity corrections for the same alignment campaigns, suggesting that the inter-release inconsistencies affect both deformation components differently.

The magnitude of these corrections further demonstrates their relevance for long-term deformation reconstruction. Considering the absolute ϑ values pooled from all three alignment operations, the 90th percentile is 0.54 mm/y for U-D and 0.92 mm/y for E-W, while the corresponding maxima reach 7.12 and 11.21 mm/y, respectively. In other words, although

90% of the estimated corrections remain below 0.54 mm/y in U-D and 0.92 mm/y in E-W directions, the upper 10% require corrections ranging from these thresholds up to 7.12 and 11.21 mm/y, respectively. These comparatively large corrections can accumulate into substantial deformation differences when propagated over multi-year intervals.

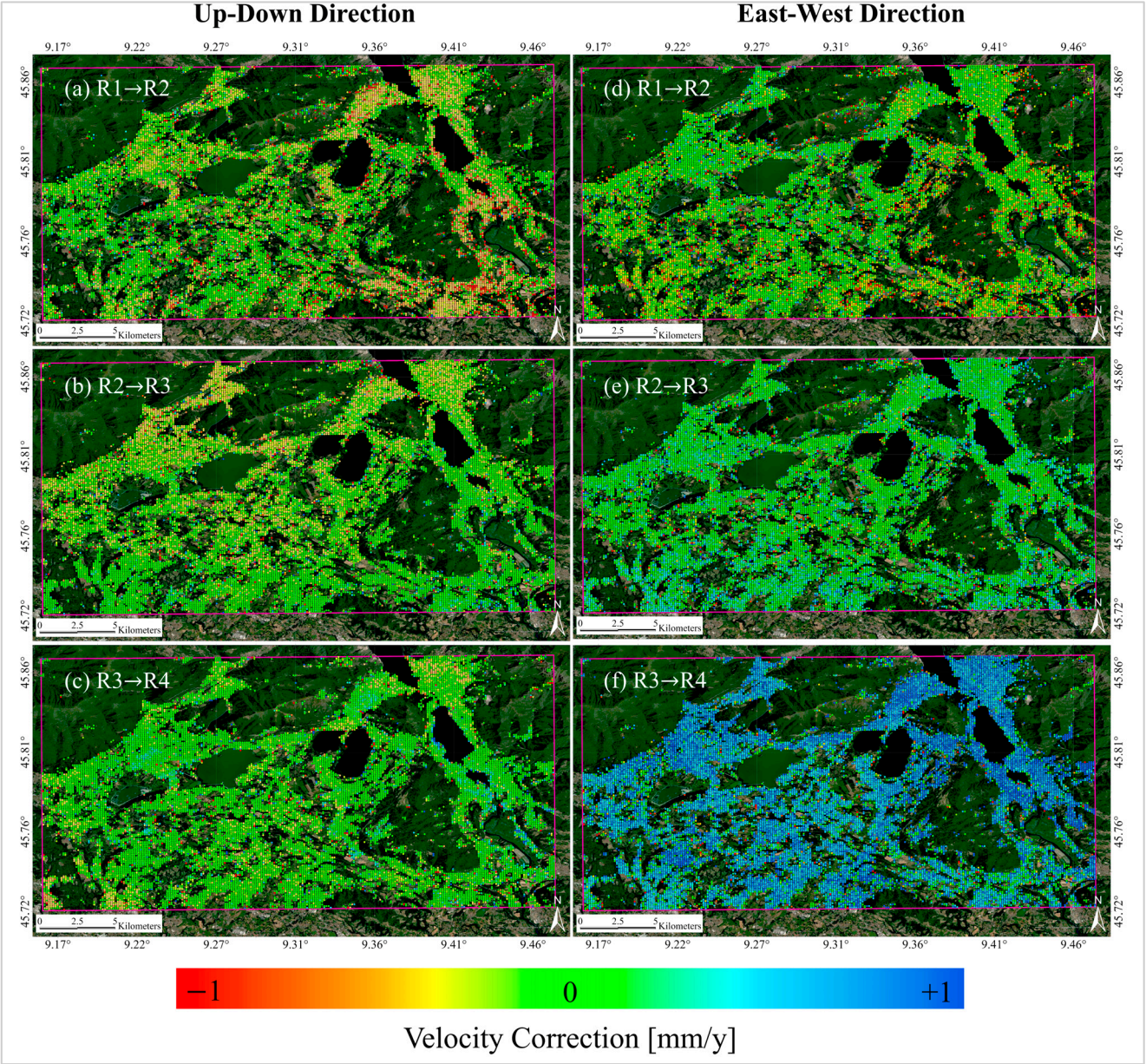

Figure 7. Spatial distribution of velocity correction [mm/y] values after temporal alignment: U-D direction [(**a**) R1 → R2; (**b**) R2 → R3; (**c**) R3 → R4] and E-W direction [(**d**) R1 → R2; (**e**) R2 → R3; (**f**) R3 → R4].

One of the main findings here, taking together these results with the single-MP example presented in Figure 5, is that all those considerable trend inconsistencies can alter the apparent long-term deformation regime if independently processed EGMS releases are directly combined. Therefore, a reliable correction for datum offsets and trend differences is an essential prerequisite for constructing temporally consistent and comparable ULT DefTS from successive EGMS Ortho releases.

4.2.3. Statistical Consistency Report

The statistical consistency of the overlapping DefTS after temporal alignment was further evaluated through the Statistical Consistency Index (SCI) introduced in Section 3.3 using Equation (10). Figure 8 presents the probability-density distributions of SCI values for the three consecutive release pairs in the U-D and E-W components (x-axis limit is set to 0.6–1 for visualization). In both directions, the distributions are strongly concentrated toward high SCI values, while elongated lower-value tails indicate a smaller subset of MPs for which greater residual distributional disagreement remains after alignment.

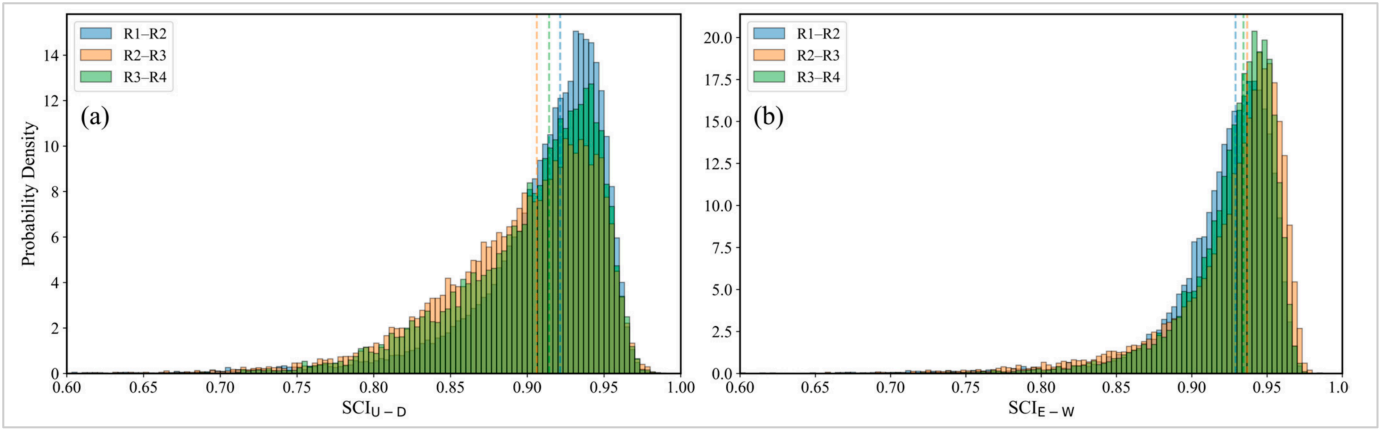

Figure 8. Probability-density distributions of the Statistical Consistency Index (SCI) after temporal alignment: (**a**) Up–Down and (**b**) East–West components.

For the U-D component (Figure 8a), all three release pairs show broadly comparable distributions, although with moderate differences in their central tendency. R1→R2 exhibits the highest median SCI of 0.921, followed by R3→R4 at 0.914 and R2→R3 at 0.906. The corresponding mean values are 0.910, 0.902, and 0.895, respectively. Most MPs retain high post-alignment consistency, with the central 80% of SCI values extending from approximately 0.856–0.951 for R1→R2, 0.827–0.949 for R2→R3, and 0.836–0.950 for R3→R4. The generally broader lower tail of R2→R3 indicates comparatively larger residual distributional discrepancies for a subset of MPs, although its upper range remains similar to the other release pairs.

The E-W component (Figure 8b) presents an even stronger concentration toward high SCI values. Median SCI values reach 0.929, 0.937, and 0.934 for R1→R2, R2→R3, and R3→R4, respectively, with the corresponding mean values of 0.921, 0.924, and 0.926. The 10–90th percentile ranges are also relatively compact, spanning 0.883–0.954, 0.873–0.960, and 0.889–0.956. Thus, despite some lower-consistency MPs represented by the extended tails, the dominant E-W population consistently exhibits SCI values above approximately 0.9.

In general, the SCI distributions demonstrate that enhanced TAST provides a high level of post-alignment distributional consistency across the consecutive EGMS releases, while also retaining sufficient sensitivity to identify MPs with comparatively larger residual disagreement. The differences among release pairs are relatively limited and do not indicate a systematic deterioration of consistency through successive releases. Moreover, the generally higher and more compact SCI distributions obtained for the E-W component indicate slightly stronger post-alignment distributional agreement than for U-D. These results complement the representative DefTS examples by providing an all-MP assessment of the internal consistency achieved after temporal alignment.

4.2.4. Analysis of Path-Dependent Alignment Discrepancies

To assess the sensitivity of the reconstructed records to the alignment path, R1 and R2 were additionally aligned directly onto R4 using enhanced TAST. The resulting translation and velocity-correction parameters, namely Γ_d and ϑ_d, were compared with their cumulative counterparts, Γ_c and ϑ_c (obtained through Equations (7) and (8)). Here, only R1→R4 and R2→R4 pairs are taken into account, with cumulative transformations comprising, respectively, three and two pairwise alignment steps; R3→R4 is ignored since its cumulative and direct alignments are identical. The comparison considered approximately 14,700 MPs with all four releases available and was performed separately for the U-D and E-W components. Translations were expressed at a common reference epoch to ensure consistent comparison. Tables 4 and 5 summarize the parameter relationships and the distributions of cumulative-direct differences.

Table 4. Comparison of cumulative and direct-to-R4 alignment parameters for the U-D component.

	Pair	Spearman q_c, q_d	MAE q_c, q_d	Mean Δq_{cd}	StD Δq_{cd}	Median $\lvert\Delta q_{cd}\rvert$	P90 $\lvert\Delta q_{cd}\rvert$
Translation Γ	R2–R4	0.90	0.46	−0.25	0.40	0.34	1.01
	R1–R4	0.91	0.58	−0.20	0.80	0.41	1.21
Velocity Correction ϑ	R2–R4	0.58	0.30	0.17	0.39	0.22	0.66
	R1–R4	0.28	0.59	0.20	0.81	0.44	1.30

[MAE: mean absolute error; StD: standard deviation; P90: 90th percentile, $q \in \{\Gamma, \vartheta\}$.]

Table 5. Comparison of cumulative and direct-to-R4 alignment parameters for the E-W component.

	Pair	Spearman q_c, q_d	MAE q_c, q_d	Mean Δq_{cd}	StD Δq_{cd}	Median $\lvert\Delta q_{cd}\rvert$	P90 $\lvert\Delta q_{cd}\rvert$
Translation Γ	R2–R4	0.87	0.56	0.21	0.75	0.43	1.19
	R1–R4	0.87	0.68	0.06	0.93	0.52	1.40
Velocity Correction ϑ	R2–R4	0.57	0.37	−0.11	0.50	0.29	0.78
	R1–R4	0.39	0.63	−0.06	0.86	0.49	1.27

[MAE: mean absolute error; StD: standard deviation; P90: 90th percentile, $q \in \{\Gamma, \vartheta\}$.]

Translation parameters exhibit strong rank agreement between the two approaches, with Spearman coefficients of 0.87–0.91. Their median absolute differences increase from 0.34 to 0.41 mm between R2→R4 and R1→R4 for U-D, and from 0.43 to 0.52 mm for E-W. Velocity corrections show greater sensitivity to the alignment path: the corresponding Spearman coefficients decrease from 0.58 to 0.28 for U-D and from 0.57 to 0.39 for E-W. Median absolute velocity differences increase from 0.22 to 0.44 mm/y for U-D and from 0.29 to 0.49 mm/y for E-W, while their 90th percentiles increase from 0.66 to 1.30 mm/y and from 0.78 to 1.27 mm/y, respectively. These results demonstrate greater cumulative-direct dispersion for the earlier release, particularly in the estimated velocity corrections.

The larger discrepancies for R1 are consistent with greater sensitivity in the longer transformation chain; however, they cannot be attributed exclusively to the number of alignment steps. It is of great importance to note that direct and cumulative estimates also exploit different overlap durations and temporal information: 4 years for sequential alignments, and only 2 and 3 years for R1→R4 and R2→R4, respectively. Neither solution constitutes an external accuracy reference. Nevertheless, the comparison quantifies the variability associated with alternative alignment paths and highlights the importance of velocity-correction differences, whose contribution to displacement disagreement scales with temporal distance from the reference epoch. The reported statistics should not be

interpreted as absolute deformation errors, since they characterize empirical path sensitivity of the alignment procedure.

4.3. Hydro-Deformation Regime Concordance Analysis

Following the construction of the ULT DefTS, a partial-trend analysis was carried out by estimating deformation velocities over the time intervals delimited by the identified GWL TPs. The corresponding velocity maps are provided in Appendix A. These successive deformation regimes were then compared with the type of hydro-regime modifications to derive the HDRC metric based on Equation (14), which expresses both the sign and magnitude of the deformation response to those variations. To illustrate how HDRC is obtained and interpreted, representative MPs and their ULT deformation histories are first examined, followed by analysis of the spatial distribution and statistical characteristics of HDRC across the AoI.

4.3.1. Temporal Evidence of the Deformation Response

Figure 9 together with Figure 10 illustrate the derivation and physical interpretation of HDRC using two representative ULT DefTS. The three GWL TPs define alternating hydrogeological regimes: TP1 and TP3 correspond to local GWL maxima (concave), whereas TP2 represents a local minimum (convex). Accordingly, the deformation response can be examined through the corresponding change in partial deformation velocity across each TP. A ULT DefTS exhibiting the same turning geometry (i.e., compatible concavity/convexity with the hydro-regime) produces a positive HDRC, while an opposite change in deformation regime produces a negative HDRC.

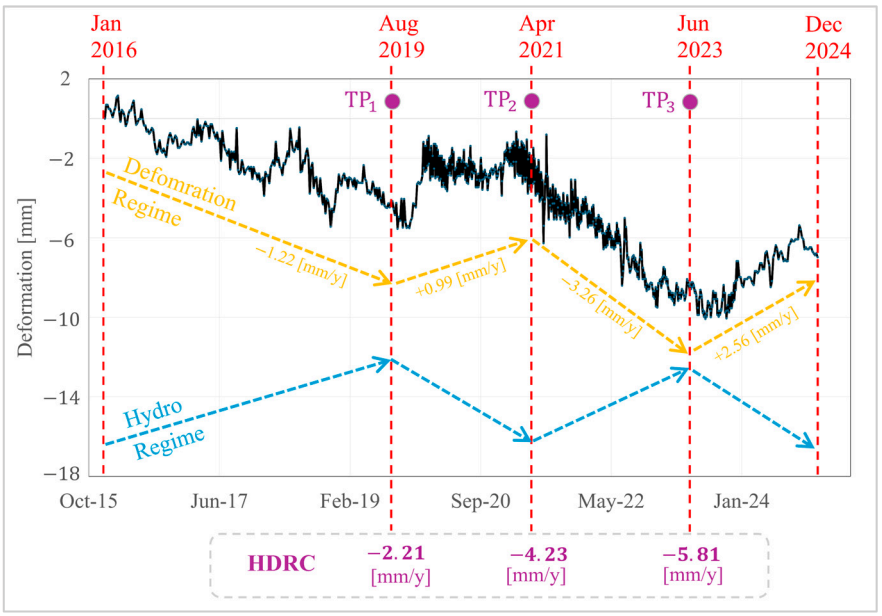

Figure 9. ULT DefTS of a representative MP (pid: 10UnVpO244), dominated by negative Hydro-Deformation Regime Concordance (HDRC).

The case in Figure 9 is dominated by negative HDRC values. At TP1, for example, the deformation velocity changes from −1.22 to +0.99 mm/y, producing an upward-turning deformation regime while the GWL changes from rising to falling; the resulting HDRC is therefore −2.21 mm/y. The same opposite-regime behavior occurs at TP2 and TP3, yielding HDRC values of −4.23 and −5.81 mm/y, respectively. The deformation evolution at this location is predominantly anti-concordant with the GWL turning behavior. Conversely, Figure 10 represents a predominantly positive HDRC response. Across TP1, the deformation

velocity changes from −1.50 to −3.43 mm/y (concave), consistent with the concave transition of GWL, giving an HDRC of +1.93 mm/y. The deformation regime also changes consistently with the hydro-regime at TP2 and TP3, producing +4.67 and +2.48 mm/y, respectively.

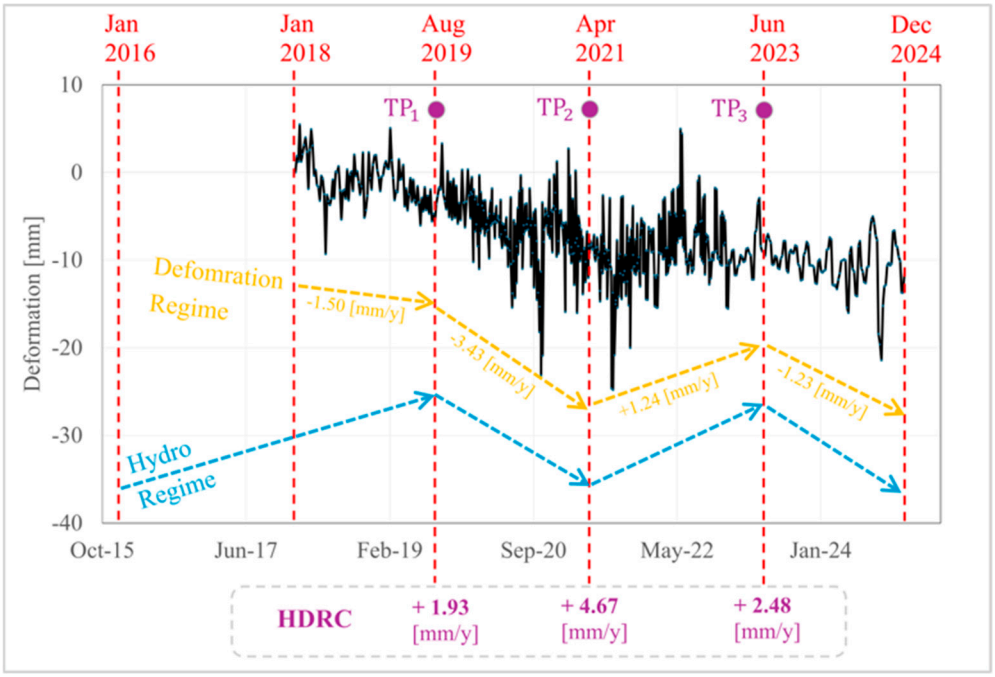

Figure 10. ULT DefTS of a representative MP (pid: 10UgTpWEvr), dominated by positive HDRC.

4.3.2. HDRC Spatial Distribution

Figures 11 and 12 show the spatial distribution of HDRC at the three TPs for the U-D and E-W components, respectively. Rather than exhibiting a spatially random mixture of positive and negative values, both components contain coherent domains of neighboring MPs with a spatially correlated HDRC sign and magnitude. This spatial integrity is particularly relevant because the HDRC sign already accounts for the direction of the hydro-regime change at each TP. Consequently, the persistence of the same HDRC sign across different TPs indicates a recurring concordant (purple colors) or anti-concordant (yellow colors) deformation response despite the alternating GWL trends.

In the U-D component (Figure 11), a comparatively persistent spatial pattern can be recognized. The south-western part of the AoI repeatedly contains predominantly positive HDRC values, indicating a recurrent concordant vertical response at all three TPs. In contrast, broad portions of the northern and north-eastern sectors are repeatedly characterized by negative HDRC, although their intensity and spatial extent vary between TPs. Notably, negative HDRC behavior can be persistently seen in areas such as the surroundings of Garlate Lake, Annone Lake's northern part (west of Valmadrera town) and the southern portion, and northern zone of Alserio Lake (center of Erba town). Between these persistent regions, near-zero and mixed-sign areas indicate locations where the deformation regime responds weakly to the identified hydro-regime modifications. Overall, the U-D maps reveal both persistent response domains and local temporal variability, rather than a single regional deformation response.

The E-W component (Figure 12) exhibits more spatially compartmentalized and temporally variable behavior. TP1 is characterized by extensive positive HDRC domains over much of the northern and central portions of the AoI, whereas TP2 shows a pronounced redistribution towards negative or weak responses in several of these areas. At TP3, contrasting positive and negative domains remain clearly distinguishable. Such spatial contrasts

suggest that the horizontal deformation response is more heterogeneous than the vertical component and that its relationship with the hydro-regime can change substantially between successive TPs. Notably, areas such as Lecco town show persistent behavior of positive HDRC with varying magnitudes, while the northern and southern high-relief areas of Valmadrera town demonstrate opposing HDRC distribution.

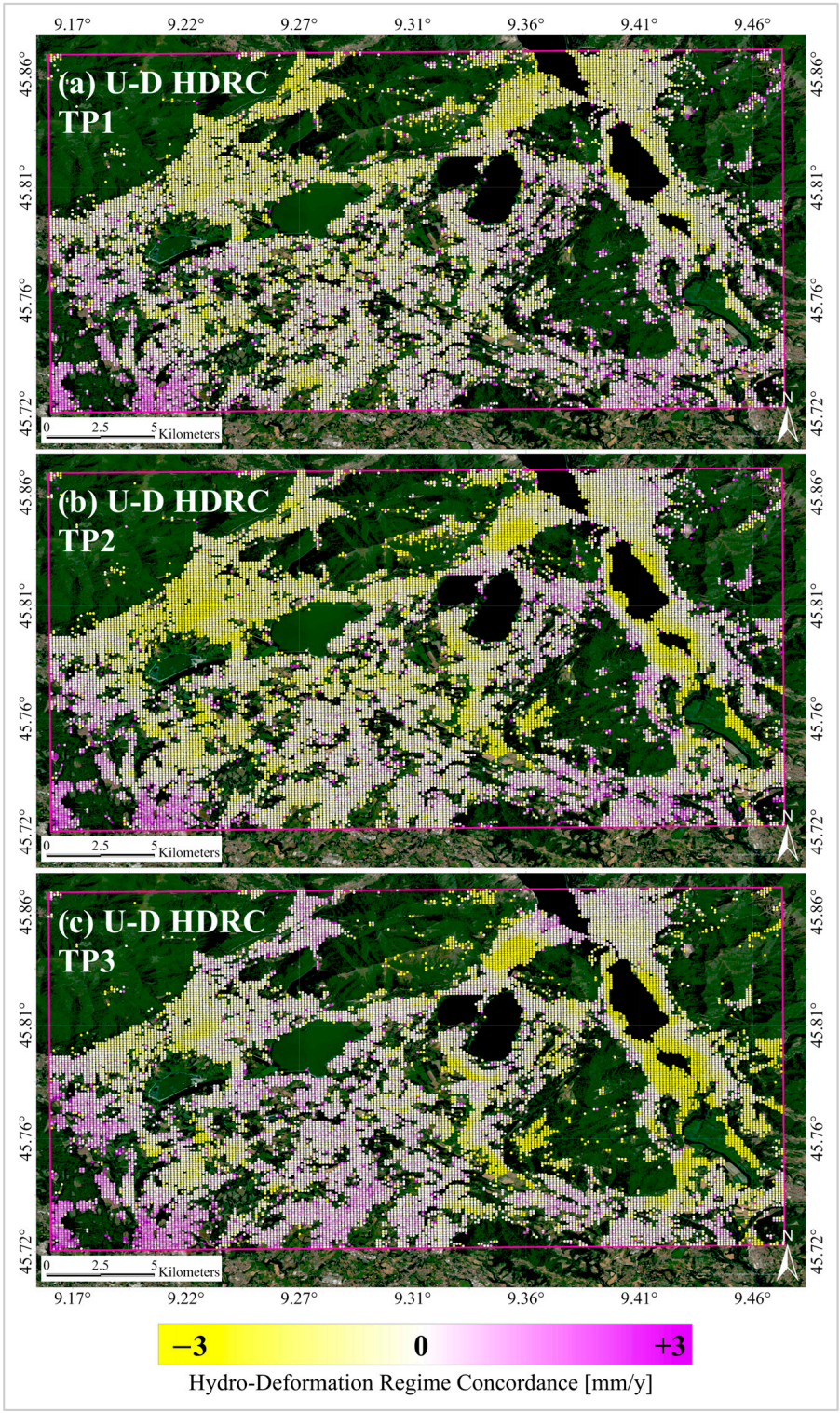

Figure 11. Maps of HDRC [mm/y] for vertical U-D direction: (**a**) turning point (TP) 1 [August 2019], (**b**) TP 2 [April 2021], and (**c**) TP 3 [June 2023].

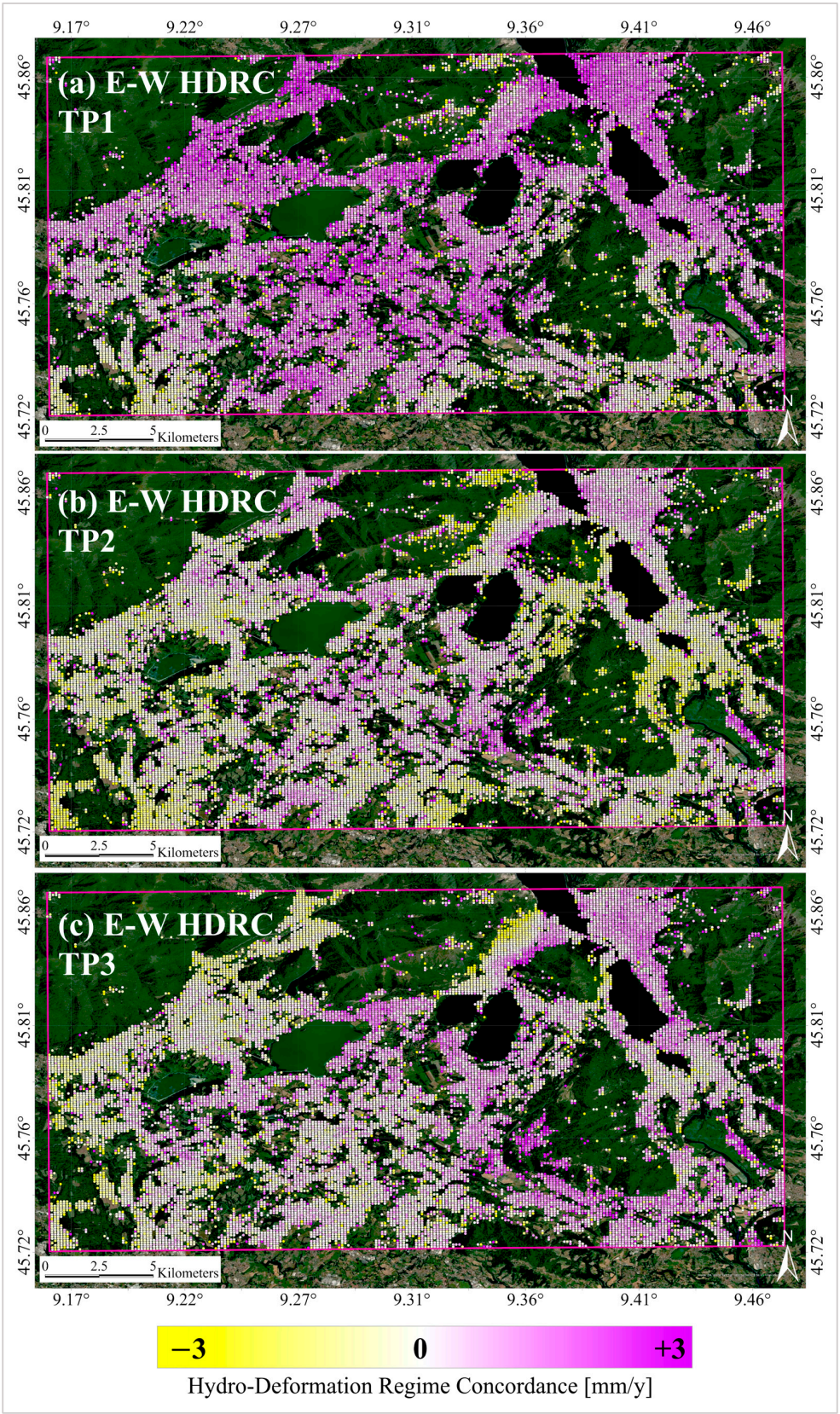

Figure 12. Maps of HDRC [mm/y] for horizontal E-W direction: (**a**) TP 1 [August 2019], (**b**) TP 2 [April 2021], and (**c**) TP 3 [June 2023].

It is evident that several local patterns retain clear spatial integrity even when their sign changes between TPs. This claim is also supported by the Moran's *I* reported at Section 4.3.3,

where the statistical prevalence and persistence of these response regimes are quantitatively examined. These indicate that the HDRC maps do not simply reflect isolated MP-level fluctuations. Instead, the hydro-deformation response appears to be spatially structured, while its temporal persistence differs across the AoI and between deformation components. The U-D component generally shows more recognizable regions of repeated concordant or anti-concordant behavior, whereas the E-W component is characterized by stronger spatial contrasts and more frequent TP-to-TP reorganization.

4.3.3. Spatial and Distributional Statistics of HDRC

To quantitatively assess the spatial organization observed in Figures 11 and 12, a global Moran's analysis was performed on the HDRC values at each TP for both deformation components. Moran's I values were calculated using a binary fixed-distance spatial-weight matrix, with MPs located within 700 m of considered neighbors. The analysis was performed in the projected ETRS89-LAEA coordinate system (EPSG:3035), and the spatial weights were row-standardized. Moreover, statistical significance was assessed using 9999 random permutations.

For the U-D component, Moran's I values increase from 0.262 at TP1 to 0.357 at TP2 and 0.508 at TP3. All three positive values indicate a tendency for MPs with similar HDRC responses to occur spatially close to one another, consistent with the coherent concordant and anti-concordant domains identified in the corresponding maps. The progressive increase towards TP3 is noteworthy, with Moran's $I = 0.508$, indicating a stronger spatial organization of the vertical hydro-deformation response at the latest TP.

The E-W component also exhibits positive spatial autocorrelation, although with systematically lower Moran's I values of 0.214, 0.182, and 0.263 for TP1, TP2, and TP3, respectively. This weaker spatial dependence agrees with the stronger local contrasts and more frequent reorganization observed in the E-W HDRC maps. Nevertheless, it does not imply that the horizontal responses are spatially random, but they form spatially organized domains, although with less regional integrity than in the U-D component. Permutation-based p-values were $\leq$0.0001 for all TPs in both U-D and E-W components. Together, these results quantitatively support the spatial patterns discussed at Section 4.3.2.

The HDRC distributions further reveal systematic differences among the TPs, as shown in Figure 13. In the U-D component, the distributions are consistently shifted towards negative values, with median HDRC values of −0.30, −0.48, and −0.19 mm/y for TP1, TP2, and TP3, respectively. Their corresponding 10–90th percentile intervals are [−1.61, +0.94], [−2.02, +0.89], and [−2.05, +0.92] mm/y. Thus, although both concordant and anti-concordant responses occur throughout the AoI, the vertical component is regionally dominated by considerable negative HDRC, particularly at TP2. A different temporal behavior characterizes the E-W component. TP1 is strongly shifted towards positive concordance, with a median of +1.07 mm/y and a 10–90th percentile interval of [−0.47, +2.32] mm/y. At TP2, the distribution becomes nearly centered on zero, with an approximately zero median and a comparatively symmetric percentile interval of [−1.37, +1.29] mm/y. At TP3, a moderate positive tendency re-emerges, with a median of +0.32 mm/y and a percentile interval of [−0.93, +1.52] mm/y. The E-W response therefore shows stronger TP-to-TP changes in its regional tendency, consistent with the spatial reorganization evident in Figure 12.

Considering the absolute HDRC magnitudes pooled across all three TPs, the 10th, 50th, and 90th percentiles are 0.13, 0.69, and 2.07 mm/y for U-D and 0.14, 0.80, and 2.13 mm/y for E-W, respectively. These results indicate broadly comparable response magnitudes in both deformation components, despite their different spatial and directional behavior. The 10th percentile absolute HDRC values of 0.13 mm/y for U-D and 0.14 mm/y for E-W are subsequently adopted in the geological conditioning analysis as magnitude-based

thresholds for separating very weak HDRC responses from the more representative hydro-deformation signal.

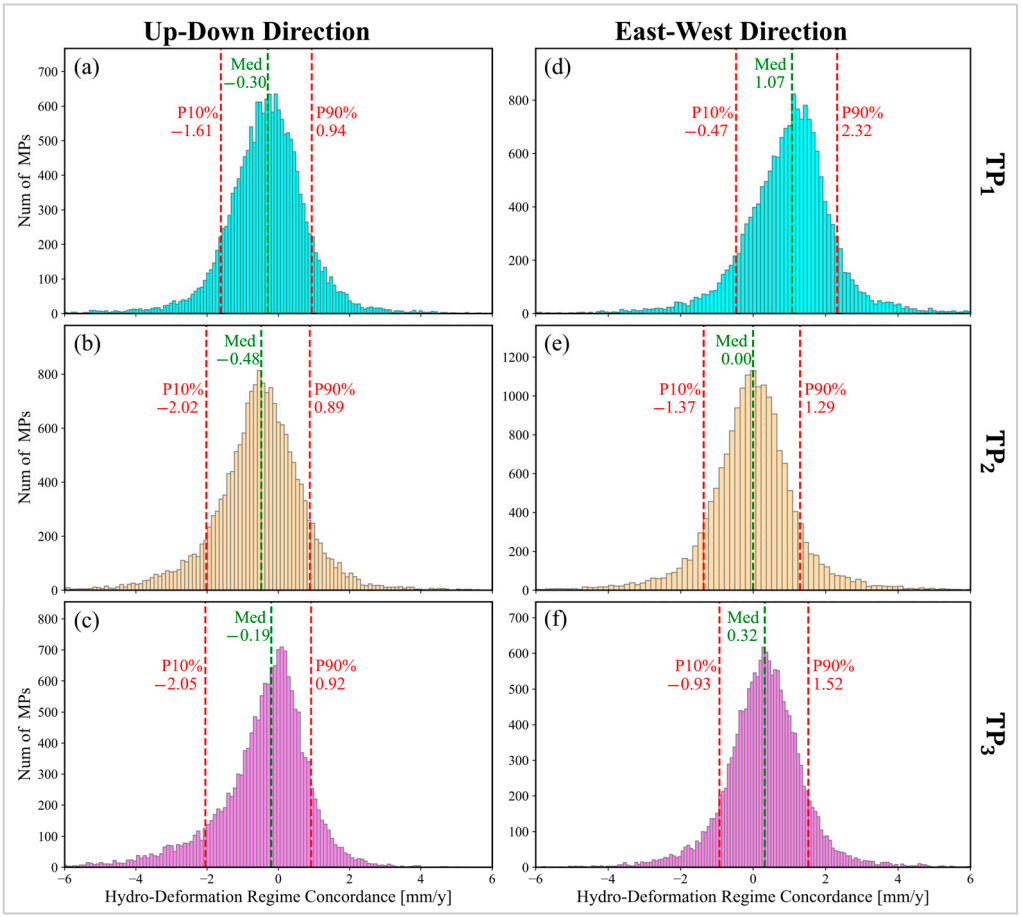

Figure 13. Distributions of HDRC values at TP1–TP3 for the U-D (**a**–**c**) and E-W (**d**–**f**) deformation components.

To further examine the dependency of the HDRC values on the selected TP dates (see Section 3.4.1), a sensitivity analysis was performed, and the results are reported in Appendix C. The statistics show that the principal HDRC and spatial-organization conclusions are stable to moderate perturbations of the TP locations. For the ±3-month shifts, HDRC vectors remained strongly associated with those obtained using the reference dates, with R^2 generally remaining high and HDRC sign-class agreement mostly around 80–92%. Larger ±6-month perturbations produced greater differences in individual HDRC magnitudes, particularly around TP3 (because TP3 is comparatively close to the December 2024 end boundary), as expected from the stronger modification of the adjacent regression intervals. Nevertheless, Moran's *I* remained positive for every tested perturbation in both deformation components, indicating that the conclusion of spatially organized HDRC patterns is not dependent on the exact adopted TP dates.

4.3.4. Regression-Based Uncertainty of Partial Velocities and HDRC

The regression-based uncertainty assessment described in Section 3.4.3 was applied to the period-wise deformation velocities and the corresponding HDRC estimates for both deformation components. Table 6 summarizes the distribution of the MP-specific standard errors (StE), reporting their median and 90th percentile (P90) for each partial deformation velocity and HDRC, adopting a 60-day Bartlett temporal bandwidth. For HDRC, the table additionally reports the percentage of estimates whose approximate pointwise 95% uncer-

tainty intervals exclude zero. Notably, these uncertainty estimates are conditional on the adopted ULT reconstruction, TP locations, and partial-trend model, and only characterize the precision of the derived deformation-regime changes.

Table 6. Conditional regression-based standard errors of period-wise deformation velocities and HDRC for the U-D and E-W components.

	Quantity	Median StE [mm/y]	P90 StE [mm/y]	95% HDRC Intervals (Excluding Zero) [%]
Up–Down Direction	$DefV_{P1}$	0.115	0.237	-
	$DefV_{P2}$	0.193	0.462	-
	$DefV_{P3}$	0.168	0.377	-
	$DefV_{P4}$	0.268	0.683	-
	$HDRC_{TP1}$	0.226	0.525	59.83
	$HDRC_{TP2}$	0.262	0.608	60.20
	$HDRC_{TP3}$	0.323	0.794	46.73
East–West Direction	$DefV_{P1}$	0.118	0.282	-
	$DefV_{P2}$	0.230	0.565	-
	$DefV_{P3}$	0.188	0.448	-
	$DefV_{P4}$	0.311	0.835	-
	$HDRC_{TP1}$	0.260	0.630	73.62
	$HDRC_{TP2}$	0.302	0.737	46.66
	$HDRC_{TP3}$	0.371	0.965	42.08

[StE: standard error; P90: 90th percentile.]

For the U-D component, the median StE of the partial deformation velocities ranges from 0.115 to 0.268 mm/y, generally increasing from P1 towards P4, while the corresponding P90 values range from 0.237 to 0.683 mm/y. The propagated HDRC uncertainties are moderately larger, with median StE values of 0.226, 0.262, and 0.323 mm/y at TP1, TP2, and TP3, respectively. Nevertheless, the approximate 95% intervals exclude zero for 59.8%, 60.2%, and 46.7% of the U-D HDRC estimates, which indicates that a substantial portion of the mapped regime changes remains distinguishable from zero after accounting for regression uncertainty. A comparable behavior is obtained for the E-W component, although, in general, the uncertainty levels are slightly larger. Median StE values of the partial velocities range from 0.118 to 0.311 mm/y, with P90 values reaching 0.835 mm/y in P4. The propagated HDRC median StE increases from 0.260 mm/y at TP1 to 0.371 mm/y at TP3, while the corresponding P90 values range from 0.630 to 0.965 mm/y. The fraction of HDRC estimates whose 95% intervals exclude zero is highest at TP1 (73.6%), and decreases to 46.7% at TP2 and 42.1% at TP3.

Furthermore, the uncertainty estimates showed limited sensitivity to the adopted Bartlett temporal bandwidth. Repeating the covariance analysis using bandwidths of 30 and 90 days, in addition to the adopted 60-day value, produced only modest variations in the HDRC standard errors. Across the three bandwidths, median HDRC standard errors varied within 0.212–0.323 mm/y for U-D and 0.248–0.371 mm/y for E-W. More importantly, the percentage of approximate 95% HDRC intervals that excluded zero remained comparatively stable, ranging from 59.8 to 61.3%, 60.2 to 61.4%, and 46.7 to 48.9% for U-D TP1–TP3, and 73.6 to 74.5%, 46.7 to 48.2%, and 41.8 to 45.2% for E-W TP1–TP3, respectively. These limited variations indicate that the principal uncertainty interpretation is not materially dependent on the selected temporal bandwidth.

These results complement the spatial and distributional analyses by quantifying the estimation precision of the deformation-regime transitions underlying HDRC. Generally, they indicate that the uncertainty of HDRC is naturally higher than that of the individual period-wise velocities because HDRC depends on the difference between two adjacent

velocity estimates. The increasing StE toward the later periods, particularly P4 and TP3, is also consistent with the shorter temporal support of the corresponding hydro-regime intervals. However, the uncertainty assessment shows that the HDRC patterns are not solely driven by poorly resolved velocity differences, particularly at U-D TP1–TP2 and E-W TP1.

4.4. Geological Conditioning of HDRC

To investigate whether the hydro-deformation response was conditioned by the mapped geological setting, the HDRC values were spatially collected according to the 14 geological groups defined in Section 2.4. The responses were separated into positive and negative populations for each turning point and deformation component. MPs with absolute HDRC values below the component-specific thresholds of 0.13 mm/y for U-D and 0.14 mm/y for E-W, respectively, were classified as neutral and excluded from this analysis. Figures 14 and 15 summarize the mean positive and negative HDRC values, together with the group median, and the relative proportions of non-neutral MPs showing positive and negative responses.

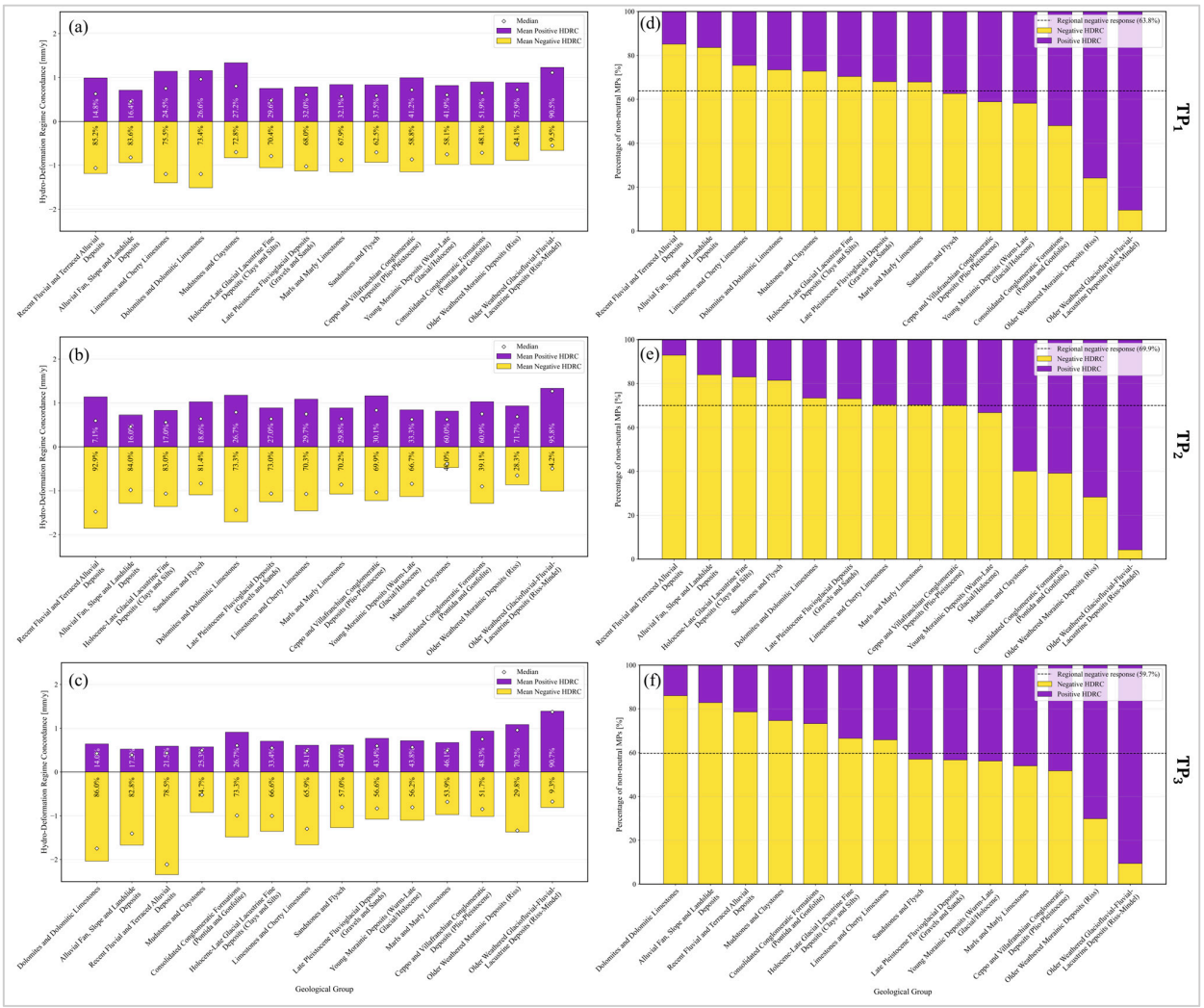

Figure 14. Geological conditioning statistics for U-D HDRC at TP1 to TP3: mean positive and negative HDRC and group medians (**a**–**c**), and proportions of non-neutral MPs showing negative or positive HDRC (**d**–**f**).

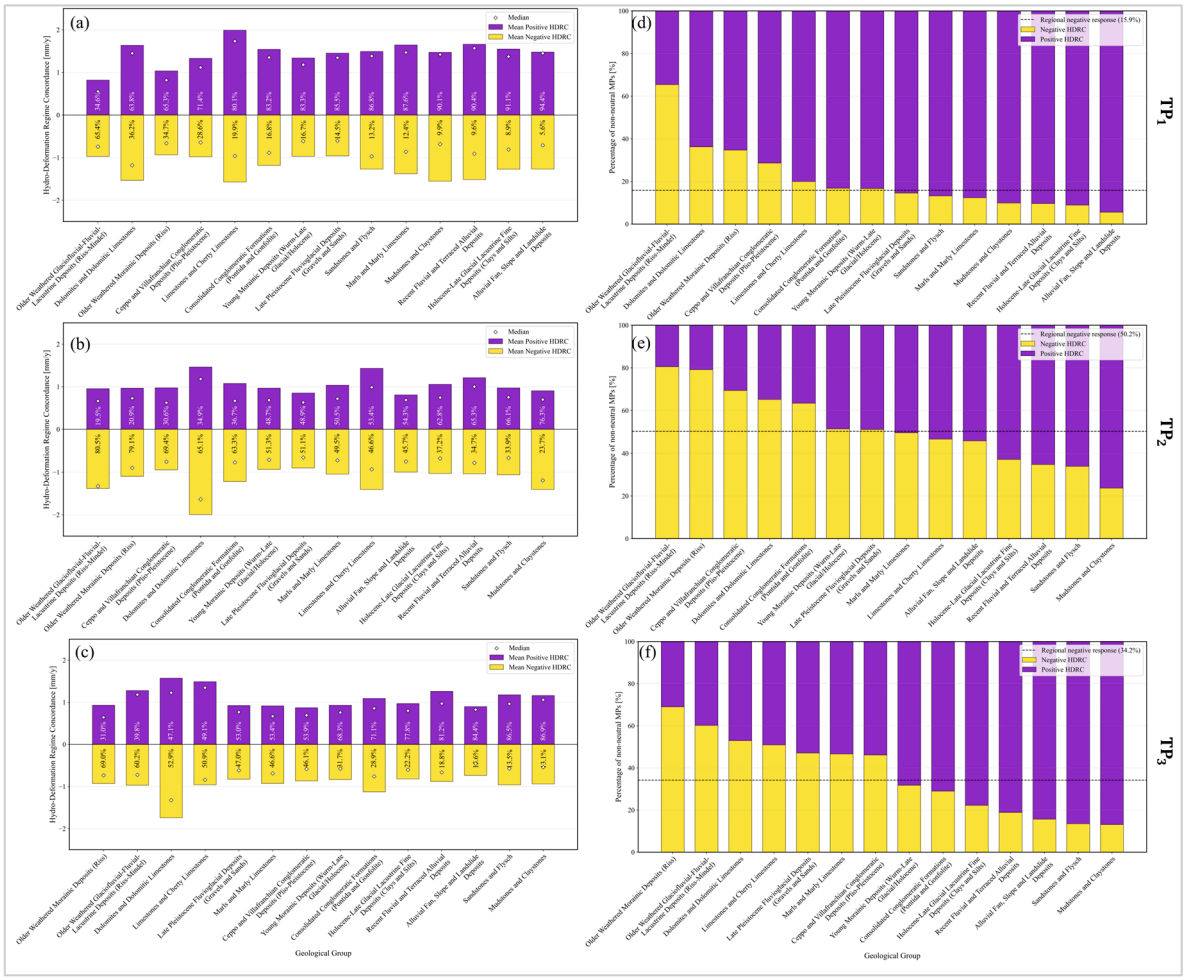

Figure 15. Geological conditioning statistics for E-W HDRC at TP1 to TP3: mean positive and negative HDRC and group medians (**a**–**c**), and proportions of non-neutral MPs showing negative or positive HDRC (**d**–**f**).

4.4.1. Vertical Deformation Response: Negative Dominance

As shown in Figure 14, for the U-D component, negative HDRC is regionally dominant, accounting for 63.8%, 69.9%, and 59.7% of the non-neutral MPs at TP1, TP2, and TP3, respectively. However, the degree of negative dominance varies considerably among geological groups, demonstrating that the regional tendency is not distributed uniformly across the AoI. Four groups exhibit a particularly persistent negative response: (i) "Recent Fluvial and Terraced Alluvial Deposits"; (ii) "Alluvial Fan, Slope and Landslide Deposits"; (iii) "Dolomites and Dolomitic Limestones"; and (iv) "Limestones and Cherty Limestones". The negative proportions in the "Recent Fluvial and Terraced Alluvial Deposits" are approximately 85.2%, 92.9%, and 78.6% at TP1-TP3, while the "Alluvial Fan, Slope and Landslide Deposits" remain remarkably stable at approximately 83–84% negative response throughout the three TPs. Both carbonate groups also remain predominantly negative, although with greater TP-to-TP variation. Moreover, the strongest negative HDRC magnitudes are repeatedly associated with "Dolomites and Dolomitic Limestones", "Limestones and Cherty Limestones", and "Recent Fluvial and Terraced Alluvial Deposits" groups, particularly at TP3.

These geological groups persistently dominated by negative U-D HDRC appear to represent two distinct hydro-mechanical settings, described as follows:

- The first comprises "Recent Fluvial and Terraced Alluvial Deposits" and "Alluvial Fan, Slope and Landslide Deposits" (i.e., unconsolidated and heterogeneous surficial materials). Such alluvial aquifer systems are particularly susceptible to deformation driven by groundwater-induced effective-stress changes, while delayed pore-pressure equilibration within fine-grained interbeds can cause deformation to lag behind changes in hydraulic head [22,43,44].
- The second setting comprises "Dolomites and Dolomitic Limestones" and "Limestones and Cherty Limestones", where deformation is less likely to arise from matrix compaction and may instead reflect groundwater-induced strain within fractured carbonate rock masses. Previous observations in carbonate aquifers show that recharge/discharge cycles and associated hydraulic-gradient changes can produce alternating compression and dilatation controlled by the fracture network [41,45].

Therefore, it is important to note that similar negative HDRC values may arise in these two geological families through fundamentally different mechanisms.

4.4.2. Vertical Deformation Response: Positive Dominance

Positive persistent behavior is observed in both older weathered Quaternary groups. The "Older Weathered Glaciofluvial–Fluvial–Lacustrine Deposits (Riss–Mindel)" exhibit positive HDRC in approximately 91%, 96%, and 91% of their non-neutral MPs at TP1–TP3, respectively, and consistently show one of the largest mean positive HDRC values. The "Older Weathered Morainic Deposits (Riss)" are also persistently positive-dominated, with positive proportions of approximately 76%, 72%, and 70%. Their persistence across all three TPs is especially relevant because the hydro-regime alternates between concave and convex transitions and the repeated response cannot be attributed solely to the direction of a particular GWL trend.

The persistently positive response of these two geological groups may be associated with their more evolved and consolidated character. The older Quaternary units comprise strongly weathered clasts and fine-grained silty–clayey matrices. In such consolidated sediments, groundwater-induced deformation can remain predominantly elastic and recoverable when effective-stress variations remain below the pre-consolidation stress [25,46]. Therefore, their recurrent positive HDRC may indicate a comparatively more reversible and temporally concordant response to GWL variations. This interpretation remains a hydro-mechanical hypothesis rather than direct evidence of the subsurface mechanism.

4.4.3. Horizontal E-W Deformation Response

The E-W results, shown in Figure 15, confirm geological differentiation, but they do not reproduce the same sign hierarchy observed for the vertical component. The regional negative proportions are only about 16% at TP1, approximately 50% at TP2, and around 34% at TP3. The horizontal response is therefore strongly positive-dominated at TP1, nearly balanced at TP2, and moderately positive-dominated at TP3.

A notable directional reversal occurs in several geological groups. The "Recent Fluvial and Terraced Alluvial Deposits" and the "Alluvial Fan, Slope, and Landslide Deposits", which are predominantly negative in U-D, are mainly positive in E-W, especially at TP1 and TP3. Their positive fractions reach approximately 90–94% at TP1 and 81–84% at TP3. Conversely, the older weathered units become among the most negative E-W groups. The "Older Weathered Glaciofluvial–Fluvial–Lacustrine Deposits (Riss–Mindel)" contain approximately 65%, 81%, and 60% negative HDRC, while the "Older Weathered Morainic Deposits (Riss)" become strongly negative at TP2 and TP3, with negative proportions of approximately 79% and 69%, respectively. The carbonate groups continue to exhibit com-

paratively large positive and negative mean HDRC magnitudes, but their sign prevalence changes considerably among TPs.

Moreover, the contrasting U-D and E-W results are of great importance and suggest component-dependent associations with the regional groundwater regime. However, as defined in Section 3.4.3, U-D HDRC relates changes in vertical deformation velocity to the direction of regional GWL transitions (i.e., compaction/expansion tendencies of the aquifer system), whereas E-W HDRC expresses only directional regime concordance. The observed E-W component depends on the orientation of local deformation relative to the east–west axis; consequently, contrasting U-D and E-W HDRC values do not necessarily indicate contradictory hydro-mechanical behavior or establish mechanical anisotropy.

4.4.4. Analysis of Geological Association and Persistence

The association between geological groups and HDRC sign was quantified using Cramér's V. The values (95% bootstrap confidence interval in brackets) for TP1, TP2, and TP3 were obtained as 0.269 [0.257, 0.285], 0.310 [0.297, 0.325], and 0.257 [0.245, 0.272] in the U-D component, respectively, while the E-W component resulted in slightly lower values of 0.237 [0.219, 0.257], 0.203 [0.190, 0.219], and 0.282 [0.268, 0.299], respectively. These magnitudes indicate a small-to-moderate association between geological settings and the occurrence of positive/negative HDRC, with the strongest dependence observed at TP2 for U-D and TP3 for E-W. The relatively similar effect sizes across three TPs suggest that the geological conditioning of deformation response is not restricted to an individual hydro-regime transition, but persists throughout the investigated period.

The temporal persistence of the geology–HDRC response was assessed by quantifying the relationship of geological-group response percentages among all possible TP pairs. Figure 16 shows these relationships for both U-D (a–c) and E-W (d–f), accompanied by the linear regression's coefficient of determination (R^2) and Spearman rank coefficient (ρ) (denoting pairwise linear and rank associations), and Kendall's coefficient of concordance (W) (indicating overall concordance across three TPs). Here, Spearman's ρ values are reported with their 95% confidence intervals in brackets. For the U-D component, where negative HDRC represents the regional dominant response, the negative-response percentages show positive associations across TPs. The strongest agreement occurs for TP1–TP2 ($R^2 = 0.76$, $\rho = 0.80$ [0.47, 0.93]) and TP1–TP3 ($R^2 = 0.78$, $\rho = 0.79$ [0.43, 0.92]), while TP2–TP3 exhibits a weaker, although still clear relationship ($R^2 = 0.47$, $\rho = 0.63$ [0.14, 0.86]). Kendall's $W = 0.83$ (p-value ≈ 0.002) indicates an overall agreement in the relative ranking of geological groups across the three hydro-regime transitions. The E-W component similarly shows persistence, and in terms of rank ordering, even stronger behavior. Positive-response percentages yield Spearman coefficients of 0.84 [0.55, 0.94], 0.80 [0.47, 0.93], and 0.83 [0.53, 0.94] for TP1–TP2, TP1–TP3, and TP2–TP3, respectively, while the corresponding R^2 values are 0.65, 0.54, and 0.69. The consistently high rank correlations, together with Kendall's $W = 0.88$ (p-value ≈ 0.001), imply that geological groups tending toward positive E-W responses generally retain their relative positions across successive TPs.

Taken together with the geological-group contrasts shown in Figures 14 and 15 and the association analysis, these results demonstrate that the HDRC response is systematically conditioned by geological setting and that this association persists across multiple GWL TPs, rather than being specific to an individual hydro-regime transition. When R^2 values are compared with ρ in all the TP pairs, it is also evident that this persistence is stronger in the relative ordering of geological responses than in their exact percentage magnitudes. Nevertheless, these patterns should be interpreted as persistent geological associations rather than direct causal attribution, since other hydrogeological, structural, and local environmental controls may contribute to the observed deformation response.

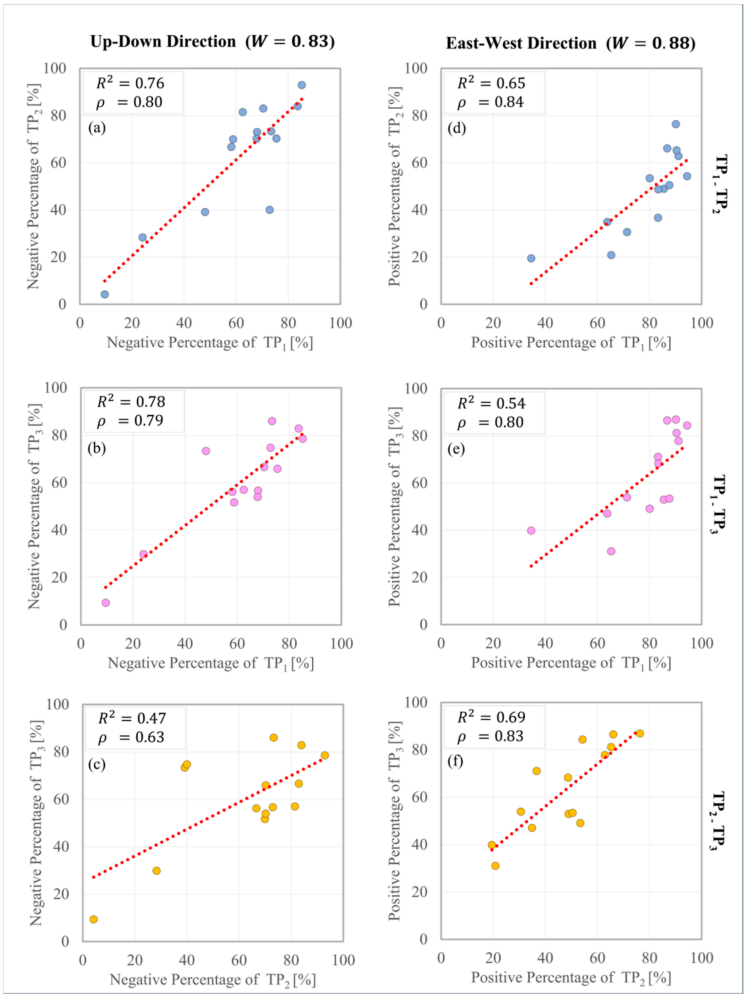

Figure 16. Persistence of geology–HDRC response among TP pairs for the U-D (**a**–**c**) and E-W (**d**–**f**) components.

Additionally, the geological-conditioning results were evaluated under the TP perturbations to demonstrate the sensitivity of these results to the TP locations, reported in Appendix C. Among the statistics, Cramér's V remained within a comparable small-to-moderate range across the tested dates, while the geological-group response patterns retained strong rank correspondence with the results obtained from reference TP dates. Spearman coefficients between perturbed and reference geological-group percentages were generally high, remaining above approximately 0.93 for most cases and above 0.74 even under the strongest perturbations. Therefore, although the exact group-wise percentages vary as the temporal segmentation is modified, the principal conclusion of persistent geological conditioning is preserved.

4.5. Assessment of Potential External Driving Factors

To increase the confidence in the association between the observed deformation dynamics and GWL variations, and to reduce the uncertainty related to potential confounding processes, other external factors capable of producing or modifying regional ground deformation were additionally screened. In particular, seismic activity, mapped faults, and extreme precipitation were considered as possible alternative or complementary drivers.

Seismic events may trigger transient or persistent deformation and, in some cases, modify pre-existing deformation processes [47–49]. A search of the USGS Earthquake Catalog [50] for the predefined vicinity of the AoI between January 2014 and December

2024 returned no seismic events potentially relevant to the observed deformation evolution. The search interval was extended two years before the beginning of the deformation analysis to account for the possibility of long-lasting post-seismic effects. In addition, inspection of the ITHACA (ITaly HAzard from CApable faults) catalog [51] maintained by Italian Institute for Environmental Protection and Research (ISPRA) revealed no mapped capable fault intersecting or immediately surrounding the AoI. ISPRA explicitly notes that ITHACA is continuously updated and is not an exhaustive inventory of all potentially capable faults in Italy. Therefore, this observation should be interpreted as the absence of currently mapped capable faults, rather than evidence for the complete absence of fault structures.

Precipitation was also examined because it represents a primary input to the regional hydrological system and may affect deformation indirectly through groundwater recharge and subsequent GWL changes and/or through changes in near-surface water storage over shorter timescales. It has been observed that extreme rainfall events may significantly alter the ground deformation patterns [12,14,52]. Figure 17 presents the daily precipitation record over the study period, extracted from VisualCrossing weather database [53], together with its 7-day moving sum. Extreme precipitation phenomena were identified using a peak-over-threshold (POT) approach, considering the 90th percentile of the 7-day moving sum precipitation series as the threshold and modelling threshold exceedances within the Generalized Pareto Distribution (GPD) framework. The resulting threshold was around 67 mm, and three main extreme-event clusters were identified in October 2018, May 2020, and May 2024. It should be noted that these are considered statistically extreme relative to the investigated 2016–2024 record, and a substantially longer precipitation record would be required to determine whether these magnitudes are exceptional in a climatological sense, which is beyond the scope of this study.

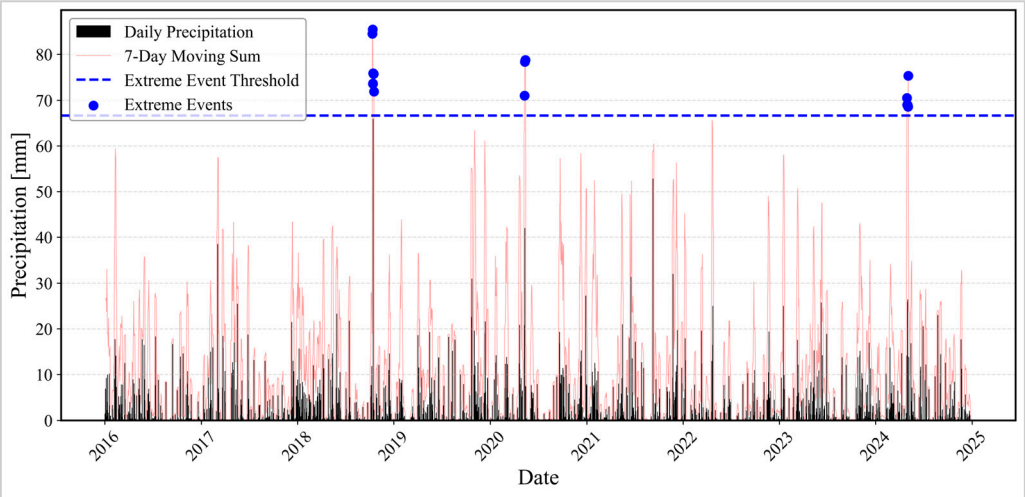

Figure 17. Daily precipitation record of AoI covering the period of study.

Nevertheless, none of the identified precipitation-event clusters coincides directly with the three GWL TPs considered for the HDRC analysis. This temporal separation provides no evidence that individual extreme rainfall episodes directly generated the investigated deformation-regime transitions. However, precipitation cannot be regarded as independent of the proposed groundwater control, since precipitation and recharge contribute to the evolution of GWL and their effects may occur with temporal delays determined by infiltration, aquifer storage, and hydraulic connectivity. Therefore, the present screening does not exclude precipitation as part of the hydrological forcing chain. However, it suggests that the GWL time series represents the more integrated hydrological state variable against which the observed multi-year deformation response can be compared.

Overall, no clear evidence was identified for seismic activity, mapped capable faulting, or isolated extreme precipitation events acting as alternative regional drivers of the multi-TP assessment of deformation pattern modifications investigated in this study. Therefore, without proving causality, these checks strengthen the interpretation of GWL variation as a principal factor associated with the observed hydro-deformation dynamics.

4.6. Limitations and Scope of Interpretation

The first group of limitations concerns the observational characteristics and constraints of Sentinel-1 InSAR and the EGMS Ortho products. Although the AoI shows generally dense and temporally persistent MP coverage, as discussed in Section 4.1, measurement availability remains dependent on radar coherence and the presence of suitable sensor-friendly targets. Consequently, decorrelated zones (such as vegetated areas) may be more sparsely represented than urban and low-relief sectors. Furthermore, the relative sensitivity to U-D and E-W deformation captured by the EGMS data depends on the acquisition geometry (with distinct uncertainty), whereas the limited sensitivity of the Sentinel-1 acquisition geometry in N-S direction is the reason that an independent N-S component cannot be retrieved. The absence of an independently resolved N-S component at the MP scale prevents determination of complete horizontal displacement, and consequently, restricts full three-dimensional interpretation.

In addition, as the present study relies on the standardized EGMS Ortho products, uncertainties inherited from the upstream MT-InSAR processing may also propagate into the reconstructed ULT DefTS. In particular, residual atmospheric-delay effects (i.e., spatially varying tropospheric contributions) in mountainous terrain, as well as possible phase-unwrapping artifacts, cannot be fully excluded, and may impose short-period or nonlinear residuals within individual releases. Therefore, release-dependent systematic offsets or trend differences may partly influence the estimated alignment corrections and be propagated through the multi-release transformation chain.

A second limitation concerns the harmonization of successive EGMS releases. As discussed in Section 3.2.2, enhanced TAST assumes that the dominant inter-release inconsistency can be represented by a translation and a linear velocity correction, where the internal nonlinear deformation variations in each release are preserved. In this way, more complex nonlinear inter-release discrepancies may remain unresolved. Moreover, since older releases are transferred to the newest-release reference frame through successive pairwise transformations, discrepancies associated with individual alignment steps may propagate towards the earlier portions of the reconstructed ULT DefTS. The comparison in Section 4.2.4 quantifies alignment-path sensitivity; for example, for R1→R4, the cumulative–direct median absolute velocity-correction differences are 0.44 mm/y for U-D and 0.49 mm/y for E-W, with corresponding 90th percentile values of 1.30 and 1.27 mm/y. However, a full uncertainty analysis would additionally require characterization of translation–velocity covariance and dependence between pairwise estimates sharing release observations. It is worth mentioning that the present validations and discrepancy analyses of this work remain mainly internal. SCI and the cumulative-versus-direct comparison assess inter-release consistency and alignment-path sensitivity, while the propagated regression uncertainties quantify uncertainty in the derived HDRC values. Independent validation against collocated GNSS/leveling observations, or through synthetic and leave-one-release-out experiments, remains an important direction for future work.

The interpretation of HDRC is additionally constrained by the available groundwater observations. The selected GWL stations exhibit a broadly coherent regional evolution and were used to identify the principal hydro-regime transitions (see Section 3.4). Therefore, instead of a direct pointwise relationship between hydraulic head and deformation, HDRC

describes the concordance between local deformation-regime modifications and the regional GWL regime. Furthermore, the lag time (i.e., delay) of spatially variable response is not explicitly estimated and may occur because of the differences in the hydraulic connectivity, the aquifer storage, and the local hydro-stratigraphy.

Likewise, the geological-conditioning results should be interpreted at the regional scale. As described in Section 2.4, the original geological units were regrouped into 14 broader groups from a 1:250,000 geological dataset, allowing statistically meaningful comparison while simplifying local subsurface variability. Parameters such as sediment thickness, aquifer geometry, hydraulic properties, fracture networks, and mechanical characteristics are not explicitly represented. Consequently, these local variations may cause different HDRC responses among MPs assigned to the same regional geological group, which can increase within-group variability and weaken the apparent geological association at the mapped scale. Furthermore, the 100 × 100 m regularization of EGMS Ortho products introduces additional spatial generalization. Overall, instead of direct evidence of a unique deformation mechanism per each geological group, the observed geological differentiation of HDRC should be interpreted as a persistent statistical conditioning by geological setting.

5. Conclusions

This study investigated the potential of successive EGMS (European Ground Motion Service) Ortho releases for constructing ultra-long-term (ULT) deformation records (i.e., continuous nominal 9-year records exceeding 5–6-year window of each single release), and for resolving non-stationary deformation behavior associated with groundwater-level (GWL) variations. An enhanced formulation of Temporal Alignment via Statistical Testing (TAST) was developed to harmonize four partially overlapping EGMS releases spanning January 2016–December 2024 while preserving the internal deformation evolution of each processing campaign. The resulting ULT deformation time series (DefTS) were subsequently analyzed across successive regional GWL regimes through the introduced Hydro-Deformation Regime Concordance (HDRC) metric, followed by spatial and geological-conditioning analyses. These two methodological advancements, i.e., enhanced TAST (for temporal harmonization) and HDRC metric (for capturing non-stationary hydro-deformation response), are the main contributions of this work. The principal findings can be summarized as follows:

- Multi-release EGMS harmonization is a crucial prerequisite for reliable ULT deformation analysis. Successive releases showed spatially coherent inter-release trend discrepancies, with velocity corrections reaching around 7 mm/y for Up–Down (U-D) and 11 mm/y for East–West (E-W). Such discrepancies can accumulate over multi-year periods and substantially modify the apparent deformation regime if releases are directly combined without temporal alignment. The SCI metric introduced in this study serves as an internal diagnostic of post-alignment statistical consistency between overlapping releases, rather than as a measure of absolute deformation accuracy. Furthermore, comparing the cumulative and direct alignment parameters revealed measurable path-dependent alignment discrepancies, with median absolute velocity-correction differences of R2→R4 with 0.22 mm/y for U-D and 0.29 mm/y for E-W, and R1→R4 with 0.44 mm/y for U-D and 0.49 mm/y for E-W.
- The harmonized records reveal distinct hydro-deformation regimes across GWL turning points (TPs). Vertical deformation was predominantly anti-concordant with the identified GWL turning behavior, with negative HDRC accounting for 59.7–69.9% of the non-neutral measurement points (MPs). In contrast, E-W responses evolved from strong positive HDRC dominance at TP1 to near-balanced conditions at TP2

and moderate positive dominance at TP3, indicating a more temporally variable directional response.

- The observed hydro-deformation responses are spatially structured rather than randomly distributed. Positive spatial autocorrelation was identified for all TPs and both components, reaching Moran's $I = 0.508$ for U-D. The vertical component generally exhibited more persistent regional domains, whereas E-W deformation showed stronger spatial compartmentalization and TP-to-TP reorganization.
- geological setting systematically conditions the sign and persistence of the deformation response. Geological association reached Cramér's $V = 0.31$, while strong agreement in geological-group response rankings across successive GWL transitions was observed, with Kendall's W reaching 0.88. Particularly persistent but contrasting responses occurred among recent alluvial deposits, carbonate formations, and older weathered Quaternary units, emphasizing that comparable HDRC behavior may arise from different hydro-mechanical settings.

Overall, this study demonstrates that the value of successive EGMS releases extends beyond periodically updated deformation maps. Once temporally harmonized, they can form a progressively expanding archive for phase-dependent investigation of long-term environmental deformation processes. The proposed framework is directly extendable to future EGMS releases and may also support investigations involving other hydrological, climatic, or geophysical drivers. Nevertheless, further developments should address nonlinear inter-release discrepancies and alignment uncertainty propagation, incorporate denser and locally representative hydrogeological observations to resolve spatially variable response delays, and exploit higher-resolution geological and hydro-mechanical information to move from statistical conditioning toward more explicit process attribution. Future developments should also complement the present internal consistency and uncertainty assessments with independent geodetic validation and controlled synthetic experiments.

Author Contributions: Conceptualization, R.E. and M.S.; Methodology, R.E. and M.S.; Resources, R.E.; Data curation, R.E.; Writing—original draft, R.E. and M.S.; Writing—review & editing, R.E. and M.S.; Visualization, R.E.; Supervision, M.S. All authors have read and agreed to the published version of the manuscript.

Funding: This research received no external funding.

Data Availability Statement: The datasets used in this study, including EGMS deformation products, groundwater-level observations, geological information, seismicity and capable-fault data, and precipitation records, are publicly available through the repositories and services cited in the corresponding sections of the manuscript. The processed datasets and derived outputs generated in this study are available from the corresponding author upon request.

Conflicts of Interest: The authors declare no conflicts of interest.

Appendix A

Figures A1 and A2 present the spatial distribution of the intermediate deformation velocities estimated through partial trend analysis for the four hydro-regime periods P1–P4, delimited by the three identified GWL TPs.

Figure A1 reports the U-D component, whereas Figure A2 shows the corresponding E-W component. The maps illustrate the spatial variability of the deformation regime across successive periods, including areas characterized by relatively persistent behavior and others exhibiting modifications in velocity magnitude or direction between periods. These partial deformation velocities constitute the intermediate quantities used to compute the velocity changes across successive TPs and, consequently, the HDRC values analyzed in Section 4.3.

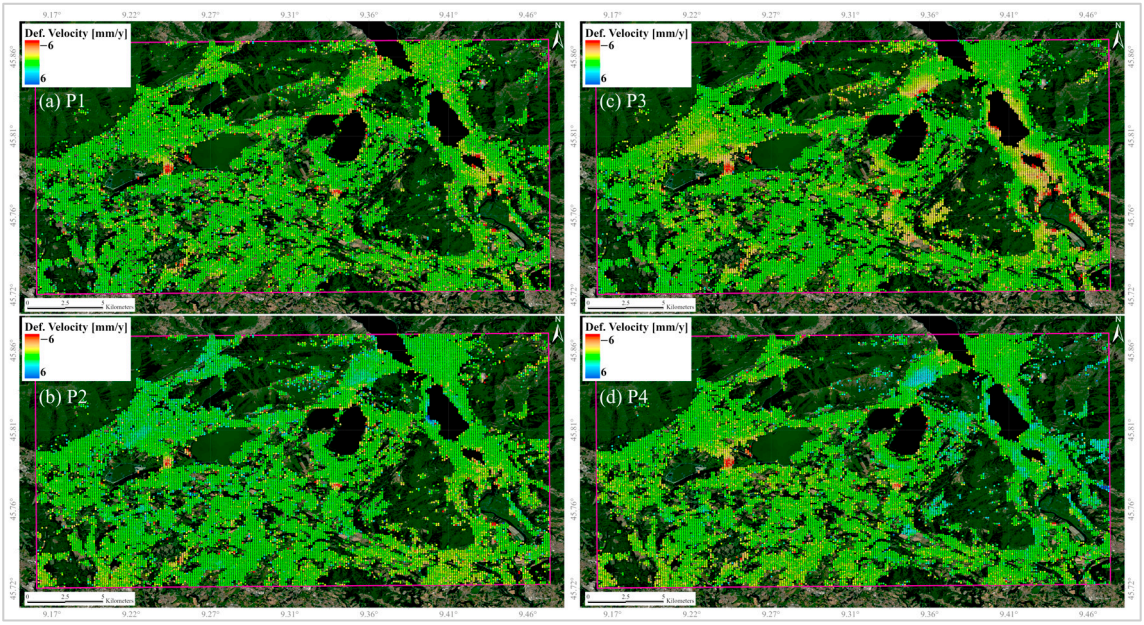

Figure A1. Spatial distribution of vertical Up–Down deformation velocity [mm/y] estimated through partial trend analysis for hydro-regime periods P1–P4 (**a**–**d**).

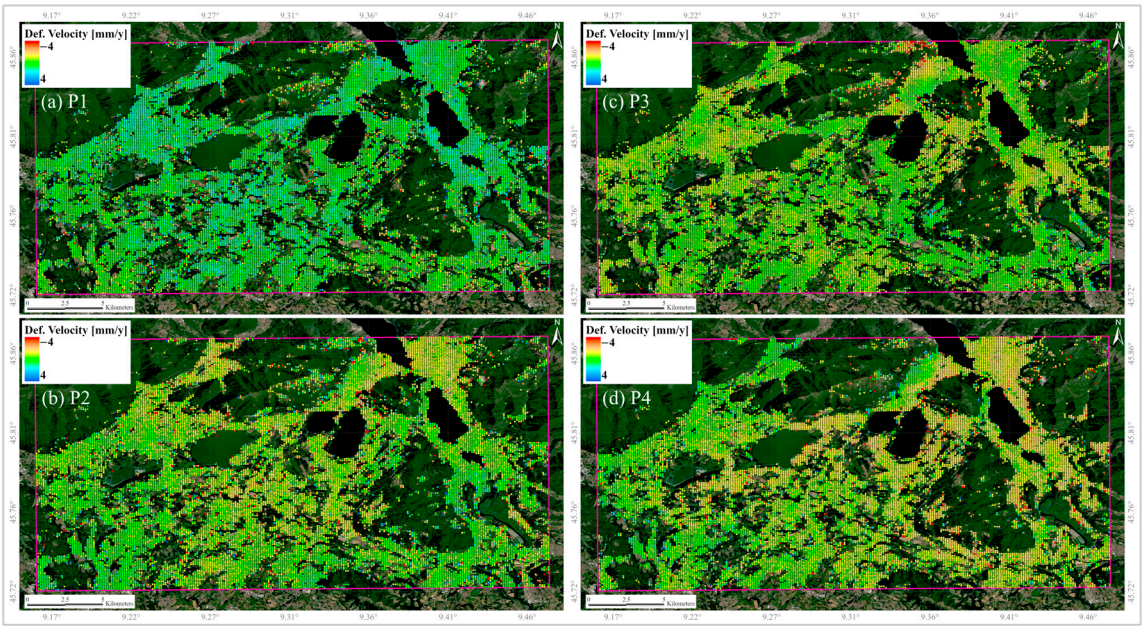

Figure A2. Spatial distribution of horizontal East–West deformation velocity [mm/y] estimated through partial trend analysis for hydro-regime periods P1–P4 (**a**–**d**).

Appendix B

To provide an objective and reproducible identification of the regional GWL turning points (TPs), a TP detection method, introduced by Eskandari and Scaioni [39] was applied (Figure A3). The approach takes advantage of the smoothed absolute difference between robust LOWESS (Locally Weighted Scatterplot Smoothing) and LOESS (Locally Estimated Scatterplot Smoothing) models to identify the occurrence and position of multiple TPs in time series.

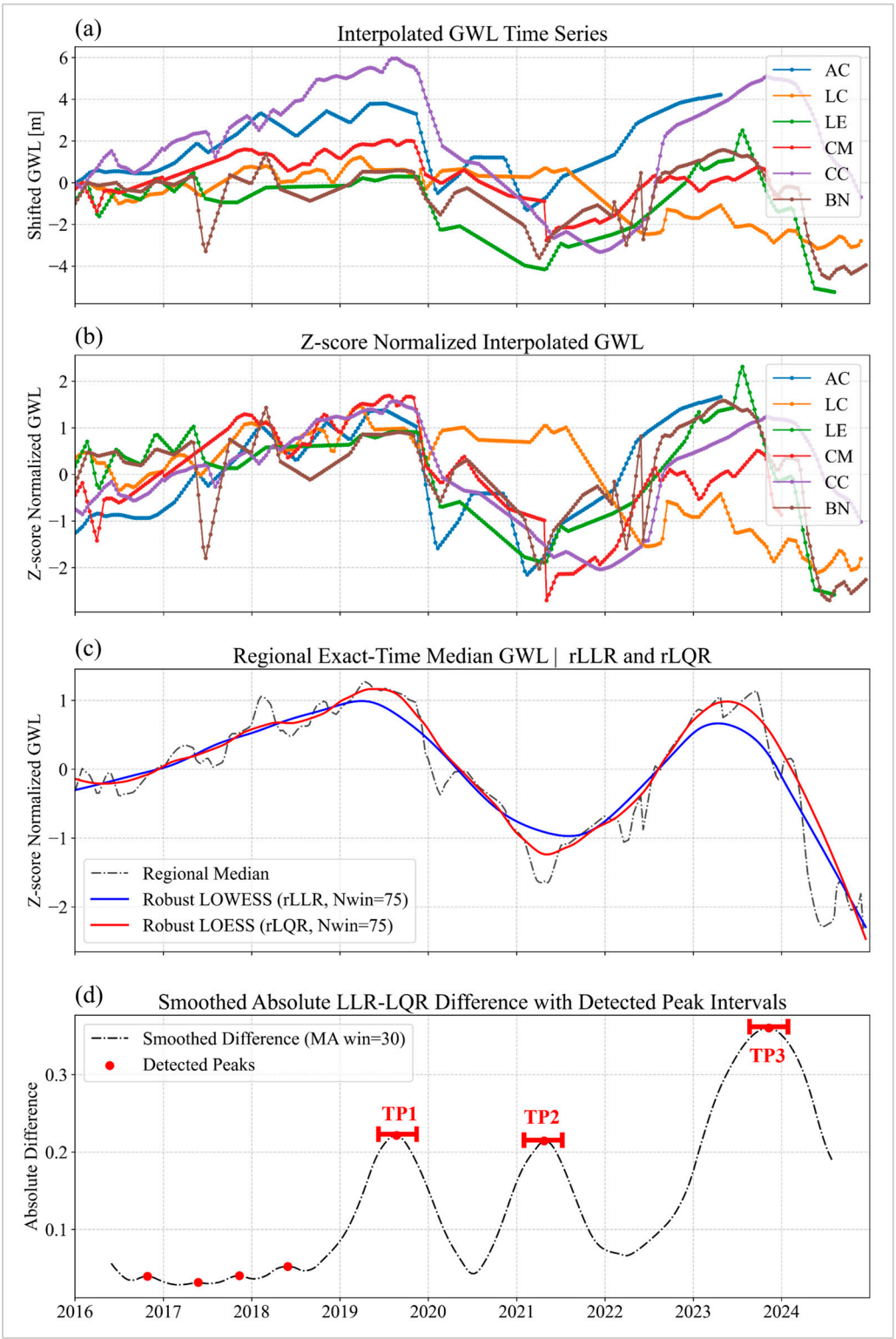

Figure A3. Objective identification of regional groundwater-level (GWL) turning points (TPs): (**a**) Relative GWL time series, linearly interpolated onto a common 10-day temporal grid; (**b**) station-wise z-score normalized interpolated GWL series; (**c**) exact-time regional median of the normalized GWL observations and corresponding robust local linear regression (rLLR) and robust local quadratic regression (rLQR); and (**d**) smoothed absolute difference between rLLR and rLQR, with the three dominant detected peaks and the adopted ±1 month TP intervals. (AC: Albese con Cassano; LC: Lecco; LE: Lurago d'Erba; CM: Costa Masnaga; CC: Calco; BN: Brenna).

First, the re-referenced (w.r.t. to their first available observation at the beginning of 2016) GWL observations of each monitoring station were linearly interpolated onto a common 10-day time vector spanning 1 January 2016–31 December 2024, without temporal extrapolation beyond the available observations of each station (Figure A3a). This was performed to address the non-uniform temporal sampling among stations. Since the objective was to identify common regional changes in GWL behavior (rather than compare absolute amplitudes among stations), each interpolated series was subsequently standardized using its station-specific mean and standard deviation (i.e., z-score normalization), as shown in Figure A3b. Then, the exact-time median of the available normalized station values was calculated to represent the regional GWL evolution in a single regional time series. TPs were identified using the procedure proposed in [39], through the smoothed absolute difference between robust LOWESS and LOESS models. In this formulation, the robust LOWESS and LOESS solutions correspond to robust local linear regression (rLLR) and robust local quadratic regression (rLQR), respectively. Both models were applied to the regional median series using a window of 75 samples, corresponding to a smoothing fraction of approximately 0.23 (Figure A3c). The absolute rLLR–rLQR difference was subsequently smoothed using a 30-sample moving average, and its peaks were examined as indicators of TP occurrence (Figure A3d).

The three dominant peaks, with distinguished prominences, associated with the principal multi-year reversals of the regional GWL trajectory correspond to TP1, TP2, and TP3. To account for the sensitivity of the exact peak position to smoothing-window selection and short-term fluctuations, a ±1 month interval was assigned around each detected peak, resulting in TP intervals of July–September 2019, March–May 2021, and May–July 2023, respectively. The central months of these intervals, i.e., August 2019, April 2021, and June 2023, were finally retained as TP1, TP2, and TP3 for the hydro-regime segmentation adopted in this study. This independent detection procedure supports the TP locations originally apparent from the regional GWL evolution and provides a reproducible basis for the temporal segmentation used in the HDRC analysis.

Appendix C

To evaluate the dependence of the HDRC-based results on the exact temporal locations of the identified GWL TPs, each TP was independently perturbed by −6, −3, +3, and +6 months while the remaining TPs were retained at their reference dates. Partial deformation velocities and HDRC were recalculated for each configuration. Tables A1 and A2 summarize the results for the U-D and E-W components, respectively.

Sensitivity of the resulting HDRC vectors was evaluated using the coefficient of determination R^2, standard deviation (StD) w.r.t the reference values, median absolute difference relative to the reference HDRC (M_A), HDRC sign-class agreement (A_C) which is percentage of MPs retaining the same positive/neutral/negative HDRC class (using the same component-specific neutral thresholds adopted in Section 4.4) relative to the reference TP, and global Moran's I (I_M). Additionally, the persistence of downstream interpretations related to geological conditioning was evaluated through Cramér's V (V_C), and agreement of response percentages with the reference solution was assessed using Spearman's rank correlation (ρ_S, negative-response percentages for U-D and positive-response percentages for E-W) and mean absolute error (MAE), both relative to the reference TP.

Table A1. Sensitivity of U-D HDRC and downstream spatial and geological statistics to perturbations of groundwater-level turning-point dates.

	Shift [Month]	HDRC Sensitivity					Geological Conditioning		
		R^2 [ ]	StD [mm/y]	M_A [mm/y]	A_C [%]	I_M [ ]	V_C [ ]	ρ_S [ ]	MAE [%]
TP1	−6	0.606	0.857	0.265	78.218	0.181	0.294	0.974	5.818
	−3	0.902	0.377	0.131	88.090	0.254	0.279	1	2.022
	0	1	0	0	100	0.262	0.269	1	0
	+3	0.909	0.371	0.146	87.444	0.133	0.244	0.930	2.213
	+6	0.694	0.744	0.293	78.655	0.186	0.211	0.938	3.872
TP2	−6	0.691	0.848	0.367	77.500	0.244	0.263	0.930	5.329
	−3	0.913	0.410	0.199	86.098	0.266	0.286	0.956	2.655
	0	1	0	0	100	0.357	0.310	1	0
	+3	0.916	0.400	0.186	87.420	0.365	0.304	0.969	2.477
	+6	0.736	0.735	0.331	80.440	0.317	0.285	0.956	6.113
TP3	−6	0.753	0.672	0.475	69.327	0.246	0.221	0.741	17.705
	−3	0.902	0.423	0.244	80.287	0.110	0.235	0.921	8.513
	0	1	0	0	100	0.508	0.257	1	0
	+3	0.870	0.511	0.256	79.671	0.524	0.287	0.974	3.001
	+6	0.479	1.298	0.665	67.076	0.414	0.287	0.969	7.052

[Parameters description: R^2: coefficient of determination; StD: standard deviation; M_A: median absolute HDRC difference; A_C: sign-class agreement; I_M: Moran's I; V_C: Cramér's V; ρ_S: Spearman correlation coefficient; MAE: mean absolute error].

Table A2. Sensitivity of E-W HDRC and downstream spatial and geological statistics to perturbations of groundwater-level turning-point dates.

	Shift [Month]	HDRC Sensitivity					Geological Conditioning		
		R^2 [ ]	StD [mm/y]	M_A [mm/y]	A_C [%]	I_M [ ]	V_C [ ]	ρ_S [ ]	MAE [%]
TP1	−6	0.585	1.026	0.353	85.552	0.142	0.240	1	5.442
	−3	0.892	0.459	0.169	91.831	0.206	0.248	1	2.287
	0	1	0	0	100	0.214	0.237	1	0
	+3	0.900	0.446	0.190	91.320	0.105	0.217	0.996	1.346
	+6	0.655	0.913	0.358	86.262	0.135	0.197	0.991	2.176
TP2	−6	0.589	1.038	0.494	70.947	0.139	0.144	0.978	8.466
	−3	0.870	0.509	0.232	81.408	0.138	0.185	0.947	4.491
	0	1	0	0	100	0.182	0.203	1	0
	+3	0.873	0.490	0.218	81.745	0.201	0.218	0.982	2.604
	+6	0.634	0.897	0.372	73.368	0.201	0.225	0.960	4.205
TP3	−6	0.579	0.774	0.401	71.079	0.091	0.197	0.925	6.73
	−3	0.817	0.495	0.246	80.503	0.047	0.220	0.987	3.866
	0	1	0	0	100	0.263	0.282	1	0
	+3	0.758	0.605	0.284	78.826	0.244	0.271	0.982	2.088
	+6	0.265	1.512	0.657	63.924	0.137	0.210	0.868	6.876

[Parameters description: R^2: coefficient of determination; StD: standard deviation; M_A: median absolute HDRC difference; A_C: sign-class agreement; I_M: Moran's I; V_C: Cramér's V; ρ_S: Spearman correlation coefficient; MAE: mean absolute error].

References

1. Bamler, R.; Hartl, P. Synthetic Aperture Radar Interferometry. *Inverse Probl.* **1998**, *14*, R1–R54. [CrossRef]
2. Ferretti, A.; Prati, C.; Rocca, F. Nonlinear Subsidence Rate Estimation Using Permanent Scatterers in Differential SAR Interferometry. *IEEE Trans. Geosci. Remote Sens.* **2000**, *38*, 2202–2212. [CrossRef]
3. Li, Z.; Wright, T.; Hooper, A.; Crippa, P.; Gonzalez, P.; Walters, R.; Elliott, J.; Ebmeier, S.; Hatton, E.; Parsons, B. Towards InSAR Everywhere, All the Time, with Sentinel-1. *Int. Arch. Photogramm. Remote Sens. Spat. Inf. Sci.* **2016**, *XLI-B4*, 763–766. [CrossRef]
4. Costantini, M.; Minati, F.; Trillo, F.; Ferretti, A.; Passera, E.; Rucci, A.; Dehls, J.; Larsen, Y.; Marinkovic, P.; Eineder, M.; et al. EGMS: Europe-Wide Ground Motion Monitoring Based on Full Resolution InSAR Processing of All Sentinel-1 Acquisitions. *IEEE Int. Geosci. Remote Sens. Symp.* **2022**, 5093–5096. [CrossRef]
5. Crosetto, M.; Solari, L. *Satellite Interferometry Data Interpretation and Exploitation: Case Studies from the European Ground Motion Service (EGMS)*, 1st ed.; Elsevier: Amsterdam, The Netherlands, 2023. [CrossRef]
6. Crosetto, M.; Cuevas-González, M.; Mróz, M.; Moldestad, D.A.; Raspini, F.; Casagli, N.; Bateson, L.; Novellino, A.; Motagh, M.; Guerrieri, L.; et al. European Ground Motion Service: A Decade of Sentinel-1 Observations. *Remote Sens. Environ.* **2026**, *339*, 115389. [CrossRef]
7. Thiéblemont, R.; Le Cozannet, G.; Nicholls, R.J.; Rohmer, J.; Wöppelmann, G.; Raucoules, D.; de Michele, M.; Toimil, A.; Lincke, D. Assessing Current Coastal Subsidence at Continental Scale: Insights from Europe Using the European Ground Motion Service. *Earth's Future* **2024**, *12*, e2024EF004523. [CrossRef]
8. Farías, C.A.; Lenardón Sánchez, M.; Bonì, R.; Cigna, F. Statistical and Independent Component Analysis of Sentinel-1 InSAR Time Series to Assess Land Subsidence Trends. *Remote Sens.* **2024**, *16*, 4066. [CrossRef]
9. Medici, C.; Becattini, F.; Dashwood, C.; Del Soldato, M.; Bianchini, S.; Bateson, L.; Lee, K.; Novellino, A. Chapter Three—On the Use of the EGMS Data for Studying Landslides in Great Britain. In *Earth Observation Applications to Landslide Mapping, Monitoring and Modeling*; Șandric, I., Ilinca, V., Chitu, Z., Eds.; Elsevier: Amsterdam, The Netherlands, 2025; pp. 71–86. [CrossRef]
10. Cuervas-Mons, J.; Domínguez-Cuesta, M.J.; Jiménez-Sánchez, M. Potential and Limitations of the New European Ground Motion Service in Landslides at a Local Scale. *Appl. Sci.* **2024**, *14*, 7796. [CrossRef]
11. Eskandari, R.; Biparvayekhiabani, S.; Genzano, N.; Castiglioni, C.A.; Scaioni, M. Spatiotemporal Evaluation of Pre-Seismic Deformation Patterns: The Case of Northern Thessaly, Greece. *Int. Arch. Photogramm. Remote Sens. Spat. Inf. Sci.* **2026**, *XLVIII-4/W18-2025*, 131–137. [CrossRef]
12. Eskandari, R.; Scaioni, M. Spatiotemporal Pattern Detection of Ground Deformations Induced by Extreme Rainfall Using InSAR EGMS: The Case of Cortina D'ampezzo after Vaia Storm. *ISPRS Ann. Photogramm. Remote Sens. Spat. Inf. Sci.* **2024**, *X-3-2024*, 131–138. [CrossRef]
13. Pirotti, F.; Toffah, F.E.; Guarnieri, A. Correlation Analysis of Vertical Ground Movement and Climate Using Sentinel-1 InSAR. *Remote Sens.* **2024**, *16*, 4123. [CrossRef]
14. Eskandari, R.; Scaioni, M. InSAR EGMS for Wide-Area Assessment of Extreme Rainfall-Related Modifications of Ground-Deformation Patterns: The Case of Vaia Rainstorm. In *Geomatics for Green and Digital Transition*; Borgogno-Mondino, E., Zamperlin, P., Eds.; Springer Nature: Cham, Switzerland, 2025; Volume 2463, pp. 46–60. [CrossRef]
15. Eskandari, R.; Scaioni, M. Joint Use of EGMS and Cosmo-SkyMed InSAR for Assessment of Ground and Structural Deformations: The Case of Como, Northern Italy. In Proceedings of the 6th Joint International Symposium on Deformation Monitoring (JISDM), Karlsruhe, Germany, 7–9 April 2025. [CrossRef]
16. Mele, A.; Crosetto, M.; Miano, A.; Prota, A. Adafinder Tool Applied to EGMS Data for the Structural Health Monitoring of Urban Settlements. *Remote Sens.* **2023**, *15*, 324. [CrossRef]
17. Basiou, E.; Castro-Melgar, I.; Kranis, H.; Karavias, A.; Lekkas, E.; Parcharidis, I. Assessment of the Ground Vulnerability in the Preveza Region (Greece) Using the European Ground Motion Service and Geospatial Data Concerning Critical Infrastructures. *Remote Sens.* **2025**, *17*, 327. [CrossRef]
18. Ruiz-Armenteros, A.M.; Marchamalo-Sacristán, M.; Lamas-Fernández, F.; Delgado-Blasco, J.M.; Jurado-Rodríguez, J.M.; Jurado-Rodríguez, D.; Bakon, M.; Lazecky, M.; Perissin, D.; Papco, J.; et al. Routine Monitoring of Hydraulic Infrastructures Using the European Ground Motion Service and Other Satellite Radar Sensors. *Procedia Comput. Sci.* **2024**, *239*, 2308–2315. [CrossRef]
19. Michalakis, I.; Loupasakis, C. Land Subsidence and Earthquake-Timed Vertical Offsets in the Messara Basin, Crete: EGMS-Based Screening for the 2021 Mw 6.0 Arkalochori Earthquake. *Land* **2026**, *15*, 545. [CrossRef]
20. Hrysiewicz, A.; Khoshlahjeh Azar, M.; Holohan, E.P. EGMS-Toolkit: A Set of Python Scripts for Improved Access to Datasets from the European Ground Motion Service. *Earth Sci. Inform.* **2024**, *17*, 3825–3837. [CrossRef]
21. Eskandari, R.; Scaioni, M. Temporal Merging of InSAR Deformation Time Series Via Statistical Testing: Application to EGMS Ortho Data. In *Geomatics for Green and Digital Transition*; Borgogno-Mondino, E., Zamperlin, P., Ganga, A., Tonolo, F.G., Eds.; Springer Nature: Cham, Switzerland, 2026; Volume 2985, *in press*.
22. Galloway, D.L.; Burbey, T.J. Review: Regional Land Subsidence Accompanying Groundwater Extraction. *Hydrogeol. J.* **2011**, *19*, 1459–1486. [CrossRef]

23. Castellazzi, P.; Martel, R.; Galloway, D.L.; Longuevergne, L.; Rivera, A. Assessing Groundwater Depletion and Dynamics Using GRACE and InSAR: Potential and Limitations. *Groundwater* **2016**, *54*, 768–780. [CrossRef] [PubMed]
24. Cui, T.; Schoning, G.; Gallagher, M.; Aghighi, M.A.; Pandey, S. A Coupled Hydro-Mechanical Modeling Framework to Concurrently Simulate Coal Seam Gas Induced Subsidence and Groundwater Impacts. *Water Resour. Res*. **2025**, *61*, e2024WR039280. [CrossRef]
25. Guzy, A.; Malinowska, A.A. State of the Art and Recent Advancements in the Modelling of Land Subsidence Induced by Groundwater Withdrawal. *Water* **2020**, *12*, 2051. [CrossRef]
26. Sun, W.; Zhou, R.; Wu, X.; Wang, T. Long-Term Surface Uplift Driven by Groundwater Recovery in Xi'an, China: InSAR Constraints on Aquifer Storage and Hydraulic Diffusivity. *Remote Sens*. **2026**, *18*, 1424. [CrossRef]
27. Bell, J.W.; Amelung, F.; Ferretti, A.; Bianchi, M.; Novali, F. Permanent Scatterer InSAR Reveals Seasonal and Long-Term Aquifer-System Response to Groundwater Pumping and Artificial Recharge. *Water Resour. Res*. **2008**, *44*, W02407. [CrossRef]
28. Ghobadi-Far, K.; Werth, S.; Shirzaei, M.; Bürgmann, R. Spatiotemporal Groundwater Storage Dynamics and Aquifer Mechanical Properties in the Santa Clara Valley Inferred from InSAR Deformation over 2017–2022. *Geophys. Res. Lett*. **2023**, *50*, e2023GL105157. [CrossRef]
29. Yu, Z.; Wang, Q.; Gong, H.; Zhou, C.; Chen, B.; Wang, Y. Multi-Scale Time Series InSAR Integrated with Ica for Deciphering the Coupling Mechanism between Groundwater Dynamics and Surface Deformation. *Land* **2025**, *14*, 971. [CrossRef]
30. Bozzano, F.; Esposito, C.; Franchi, S.; Mazzanti, P.; Perissin, D.; Rocca, A.; Romano, E. Understanding the Subsidence Process of a Quaternary Plain by Combining Geological and Hydrogeological Modelling with Satellite InSAR Data: The Acque Albule Plain Case Study. *Remote Sens. Environ*. **2015**, *168*, 219–238. [CrossRef]
31. Liu, S.-M.; Bai, M.-Z. Groundwater Level Rise and Geological Structure Influences on Land Deformation Dynamics: Insights from Managed Aquifer Recharge Operations in Beijing, China. *Front. Earth Sci*. **2024**, *12*, 1469772. [CrossRef]
32. Binda, G.; Frascoli, F.; Spanu, D.; Ferrario, M.F.; Terrana, S.; Gambillara, R.; Trotta, S.; Noble, P.J.; Livio, F.A.; Pozzi, A.; et al. Geochemical Markers as a Tool for the Characterization of a Multi-Layer Urban Aquifer: The Case Study of Como (Northern Italy). *Water* **2022**, *14*, 124. [CrossRef]
33. Schiavo, M. Improved Groundwater Modeling by Incorporating Geological Information from Hydrogeological Sections. *Acque Sotter.-Ital. J. Groundw*. **2023**, *12*, 9–17. [CrossRef]
34. Crosetto, M.; Solari, L.; Balasis-Levinsen, J.; Casagli, N.; Frei, M.; Oyen, A.; Moldestad, D.A. Ground Deformation Monitoring at Continental Scale: The European Ground Motion Service. *Int. Arch. Photogramm. Remote Sens. Spat. Inf. Sci*. **2020**, *XLIII-B3-2020*, 293–298. [CrossRef]
35. European Ground Motion Service (EGMS). Available online: https://egms.land.copernicus.eu/ (accessed on 5 June 2026).
36. ARPA Lombardia. Available online: https://www.arpalombardia.it/ (accessed on 9 June 2026).
37. Geoportale Della Lombardia. Available online: https://www.geoportale.regione.lombardia.it/ (accessed on 15 June 2026).
38. Engmann, S.; Cousineau, D. Comparing Distributions: The Two-Sample Anderson-Darling Test as an Alternative to the Kolmogorov-Smirnoff Test. *J. Appl. Quant. Methods* **2011**, *6*, 1–17.
39. Eskandari, R.; Scaioni, M. Automatic Detection of Turning Points for Partial Trend Analysis in InSAR Deformation Time Series: EGMS Ortho Products. In *International Association of Geodesy Symposia*; Freymueller, J.T., Sánchez, L., Eds.; Springer: Berlin/Heidelberg, Germany, 2026; pp. 1–9. [CrossRef]
40. Burbey, T.J. The Influence of Geologic Structures on Deformation Due to Ground Water Withdrawal. *Groundwater* **2008**, *46*, 202–211. [CrossRef] [PubMed]
41. Amoruso, A.; Crescentini, L.; Martino, S.; Petitta, M.; Tallini, M. Correlation between Groundwater Flow and Deformation in the Fractured Carbonate Gran Sasso Aquifer (Infn Underground Laboratories, Central Italy). *Water Resour. Res*. **2014**, *50*, 4858–4876. [CrossRef]
42. LeKhac, N.; Wu, B.; Chen, C.; Kechadi, M.T. Feature Selection Parallel Technique for Remotely Sensed Imagery Classification. In *Computational Science and Its Applications—ICCSA 2013*; Murgante, B., Misra, S., Carlini, M., Torre, C.M., Nguyen, H.-Q., Taniar, D., Apduhan, B.O., Gervasi, O., Eds.; Springer: Berlin/Heidelberg, Germany, 2013; pp. 623–634.
43. Hoffmann, J.; Galloway, D.L.; Zebker, H.A. Inverse Modeling of Interbed Storage Parameters Using Land Subsidence Observations, Antelope Valley, California. *Water Resour. Res*. **2003**, *39*, 1031. [CrossRef]
44. Carlson, G.; Shirzaei, M.; Ojha, C.; Werth, S. Subsidence-Derived Volumetric Strain Models for Mapping Extensional Fissures and Constraining Rock Mechanical Properties in the San Joaquin Valley, California. *J. Geophys. Res. Solid Earth* **2020**, *125*, e2020JB019980. [CrossRef] [PubMed]
45. Amoruso, A.; Crescentini, L.; Petitta, M.; Tallini, M. Parsimonious Recharge/Discharge Modeling in Carbonate Fractured Aquifers: The Groundwater Flow in the Gran Sasso Aquifer (Central Italy). *J. Hydrol*. **2013**, *476*, 136–146. [CrossRef]
46. Bonì, R.; Cigna, F.; Bricker, S.; Meisina, C.; McCormack, H. Characterisation of Hydraulic Head Changes and Aquifer Properties in the London Basin Using Persistent Scatterer Interferometry Ground Motion Data. *J. Hydrol*. **2016**, *540*, 835–849. [CrossRef]
47. Eskandari, R.; Genzano, N.; Scaioni, M. Deformation Pattern Modifications Induced by 2021 Brentonico Earthquake: Insights from EGMS Ortho Products. *Int. Arch. Photogramm. Remote Sens. Spat. Inf. Sci*. **2026**, *XLIX-B3-2026*, 501–507. [CrossRef]

48. Banko, A.; Pavasović, M. Fault-Parallel Postseismic Afterslip Following the 2020 Mw 6.4 Petrinja–Pokupsko Earthquake from Sentinel-1 SBAS Time Series. *Remote Sens*. **2026**, *18*, 828. [CrossRef]
49. Pawłuszek-Filipiak, K.; Wielgocka, N.; Rudziński, Ł. The Detectability of Post-Seismic Ground Displacement Using DInSAR and SBAS in Longwall Coal Mining: A Case Study in the Upper Silesian Coal Basin, Poland. *Remote Sens*. **2024**, *16*, 2533. [CrossRef]
50. U.S. Geological Survey. Earthquakes. Available online: https://earthquake.usgs.gov/earthquakes/ (accessed on 29 June 2026).
51. ITHACA (Italy Hazard from Capable Faulting). Available online: https://sgi.isprambiente.it/ithacaweb/ (accessed on 1 July 2026).
52. Shi, X.; Wang, J.; Jiang, M.; Zhang, S.; Wu, Y.; Zhong, Y. Extreme Rainfall-Related Accelerations in Landslides in Danba County, Sichuan Province, as Detected by InSAR. *Int. J. Appl. Earth Obs. Geoinf.* **2022**, *115*, 103109. [CrossRef]
53. Visual Crossing | Global Weather Data & Developer APIs. Available online: https://www.visualcrossing.com/ (accessed on 1 July 2026).

Disclaimer/Publisher's Note: The statements, opinions and data contained in all publications are solely those of the individual author(s) and contributor(s) and not of MDPI and/or the editor(s). MDPI and/or the editor(s) disclaim responsibility for any injury to people or property resulting from any ideas, methods, instructions or products referred to in the content.